

Summary

2	1	Introduction	3
3	2	Pixel detectors	5
4	2.1	Signal formation	5
5	2.2	CCDs	6
6	2.3	Hybrid pixels	6
7	2.4	CMOS MAPS and DMPAS	7
8	2.4.1	DMAPS: large and small fill factor	8
9	2.4.2	A modified sensor	9
10	2.5	Analog front end	9
11	2.5.1	Preamplifier	9
12	2.6	Readout logic	11
13	3	Use of pixel detectors	14
14	3.1	Tracking in HEP	14
15	3.1.1	Hybrid pixels at LHC and at SuperKEKB	15
16	3.1.2	First attempts to MAPS	16
17	3.2	Other applications	17
18	3.2.1	Applicability to FLASH radiotherapy	18
19	4	TJ-Monopix1	22
20	4.1	The sensor	23
21	4.2	Front end	25
22	4.2.1	ALPIDE-like	25
23	4.3	Readout logic	26
24	5	Arcadia-MD1	29
25	5.1	The sensor	29
26	5.2	Readout logic and data structure	29
27	5.2.1	Matrix division and data-packets	29
28	6	Threshold and noise characterization	33
29	6.1	TJ-Monopix1 characterization	33
30	6.1.1	Threshold and noise: figure of merit for pixel detectors	33
31	6.1.2	Calibration of the ToT	35
32	6.2	Fe vs bias	35
33	6.3	Measurements with radioactive sources	36
34	6.3.1	Dead time measurements	37
35	6.4	ARCADIA-MD1 characterization	38
36	7	Test beam measurements	40
37	7.1	Testbeam motivation	40
38	7.2	Apparatus description	40
39	7.3	Measurements	40
40	A	Pixels detector: a brief overview	42
41	A.1	Radiation damages	42

⁴² **Bibliography**

⁴⁴

⁴³ Characterization of monolithic CMOS pixel sensors for charged particle detectors and for high
⁴⁴ intensity dosimetry

⁴⁵ **Chapter 1**

⁴⁶ **Introduction**

⁴⁷ Pixel detectors, members of the semiconductor detector family, have significantly been used at the
⁴⁸ accelerator experiments for energy and position measurement. Because of their dimension (today
⁴⁹ $\sim 30 \mu\text{m}$ or even better) and their spatial resolution ($\sim 5\text{-}10 \mu\text{m}$), with the availability of technology
⁵⁰ in 1980s they proved to be perfectly suitable for vertex detector in the inner layer of the detector.

⁵¹ Despite the monolithic pixels came up with CCDs, invented in 1969 and fastly used in cameras,
⁵² their usage had to wait for microelectronics developement: in MAPS device the readout electronics
⁵³ is build on the pixel's area, then the pixel dimension is limited by the dimension of transistors. This
⁵⁴ constraint favoured the usage in physics experiment of hybrid pixels, which currently constitute
⁵⁵ the state-of-art for large scale pixel detector. These ones are made by two different wafer each one
⁵⁶ containing or the sensor or the ASIC, which are after joined together through microconnection.
⁵⁷ This structure allows a separate optimization for the two components and makes hybrid pixels
⁵⁸ flexible and versatile.

⁵⁹ Requirement imposed by accelerator are stringent and they will be even more with the increase
⁶⁰ of luminosity in terms of radiation hardness, efficiency and occupancy, time resolution, material
⁶¹ budget and power consumption. For this reason experiments (as ATLAS, CMS, BelleII) began to
⁶² look at the more innovative and well-performing monolithic active pixels (MAPS) as perspective for
⁶³ their future upgrades.

⁶⁴ Che condiziona la risoluzione e l'efficienza di ricostruzione della sua traccia, e consumi del
⁶⁵ detector, sono diventati sempre più rilevanti; molti esperimenti (ATLAS, CMS, BelleII,..) stanno
⁶⁶ infatti valutando la possibilità di sostituire gli ibridi con i MAPS, che per i temi precedenti offrono
⁶⁷ prestazioni migliori, a scapito di tempi di lettura mediamente più lunghi, vista anche la positiva
⁶⁸ esperienza di ALICE ad LHC, primo esperimento ad introdurre un detector a pixel monolitico.

⁶⁹ During my thesys I studied and characterised two monolithic active pixel chips, TJ-Monopix1
⁷⁰ and MD1; this devices, that are still prototypes, have been conceived and designed for physics
⁷¹ experiments at colliders, space experiments and also for medical applications.

⁷² il primo, TJ-Monopix1, è un prototipo di un modello selezionato per l'upgrade di Belle II
⁷³ durante il LSD nel 2025 (il chip finale si chiamerà OBELIX e avrà come sensore TJ-Monopix2,
⁷⁴ successore di Monopix1); il secondo chip è stato progettato da ARCADIA che potrà avere, nelle
⁷⁵ versioni future, applicazioni in fisica medica, in esperimenti nello spazio e ai collider.

⁷⁶ Le differenze principali tra i due chip risiedono nel segnale fornito in output (Monopix fornisce il
⁷⁷ tempo sopra soglia dell'impulso triangolare, proporzionale alla carica rilasciata nel sensore, mentre
⁷⁸ arcadia fornisce un segnale puramente digitale), nella sequenza di readout dei pixel (monopix ha
⁷⁹ una lettura puramente sequenziale di tipo "column drain") mentre arcadia ha una lettura più
⁸⁰ moderna che consente di poter aggregare dati durante la trasmissione (ad esempio nel caso di
⁸¹ formazione di cluster e creazione di hti su pixel adiacenti).

⁸² I performed a threshold and noise characterization ($\sim 400 \text{ e}^-$ and $\sim 15 \text{ e}^-$) of TJ-Monopix1 in
⁸³ order

⁸⁴ Tra i test con Monopix1 ho effettuato una caratterizzazione in soglia ($\sim 400 \text{ e}^-$) e rumore (\sim
⁸⁵ 15 e^-) al fine di visualizzare la dispersione di questi valori sulla matrice; per poter minimizzare la
⁸⁶ dispersione sulla matrice e avere una più uniforme selezione della soglia (che è globale su tutta
⁸⁷ la matrice), le versioni successive di TJ-Monopix1 includono e includeranno la possibilità di fare
⁸⁸ piccole correzioni (3 bit per pixel vengono allocati in Monopix2) di quest'ultima pixel per pixel.
⁸⁹ Per poter fornire le misure dei segnale fornito, tempo sopra soglia ToT, in elettroni, che assieme

90 alle lacune vengono create dal passaggio della particella incidente e che quindi sono la quantità
91 fisica "importante" nella misura, è stata necessaria una calibrazione assoluta dell'oggetto. Per
92 quest'ultima e per altri test ?? mi sono servita di sorgenti radiattive come il ferro 55 (emissione di
93 un fotone gamma a 5.9 kev e dello stronzio 90 il cui spettro dell'elettrone emesso ha un end point
94 a x) e dei cosmici. Inoltre ho partecipato ai test di Monopix1 su fascio: abbiamo testato il chip in
95 una modalità diversa da quella per cui è stato progettato (tracking) e più simile al funzionamento
96 delle CCD, in cui non si cerca di distinguere il singolo elettrone incidente ma si integra in un
97 singolo segnale di output la carica rilasciata da più elettroni incidenti. Il fascio utilizzato (elettroni
98 da 7-9 MeV) è un fascio ad altissima intensità e verrà utilizzato per fare ricerca su radioterapia
99 ad alto rate (l'acceleratore è in grado di rilasciare dosi -con riferimento in acqua- fino a 40 Gy/s,
100 corrispondenti ad un numero di particelle di ..). Per quanto riguarda, invece, le misure sul chip
101 MD1, ho partecipato ai test elettrici e sul front end di un prototipo non ancora completamente
102 funzionante. Un nuovo chip dovrebbe arrivare nei prossimi giorni a Pisa.

¹⁰³ **Chapter 2**

¹⁰⁴ **Pixel detectors**

¹⁰⁵ I pixel detector fanno parte della famiglia dei detector a semiconduttore e il loro funzionamento si
¹⁰⁶ basa sulla creazione di coppie elettrone lacuna all'interno del bulk. Dalla creazione della particella
¹⁰⁷ incidente di queste coppie e facendole driftare attraverso l'applicazione di un campo elettrico, si
¹⁰⁸ ottiene quindi un segnale all'interno del rivelatore correlabile all'energia della particella incidente.
¹⁰⁹ Il campo elettrico applicato, lo spessore della zona di svuotamento, le modalità con cui il
¹¹⁰ segnale viene processato e trasmesso all'esterno del rivelatore sono caratteristiche specifiche del
¹¹¹ tipo di chip. In questo capitolo tratterò dunque i principali tipi di rivelatori a pixel, sofferandomi
¹¹² in particolare sui pixel monoliti.

¹¹³ **2.1 Signal formation**

¹¹⁴ When a charge particle passes through a pixel and loses energy by ionization a part of that
¹¹⁵ energy is used to generate electron-hole pairs (another part is used for other processes, as the
¹¹⁶ lattice excitation) which are then separated by the electric field and collected at their respectively
¹¹⁷ electrodes (*p* for holes and *n* for electrons)¹; by the drift of these charges, a signal i_e is generated
¹¹⁸ on the electrode *e* as stated by the Shockley-Ramo's theorem:

$$i_e(t) = -q v(t) E_{WF,e} \quad (2.1)$$

¹¹⁹ where $v(t)$ is the instantaneous velocity of the charge q and E_{WF} is the weighting field, that is the
¹²⁰ field obtained biasing the electrode *e* with 1V and all the others with 0V. The drift velocity of the
¹²¹ charge depends on the electric field and on the mobility of the particle:

$$v = \mu(E) E \quad (2.2)$$

¹²² where $\mu(E)$ is a function of the electric field and is linear with E only for small E : at higher values
¹²³ the probability of interactions with optical phonons increases and the mobility drops and this leads
¹²⁴ to an independence of the velocity from the electric field (fig. 2.1b).

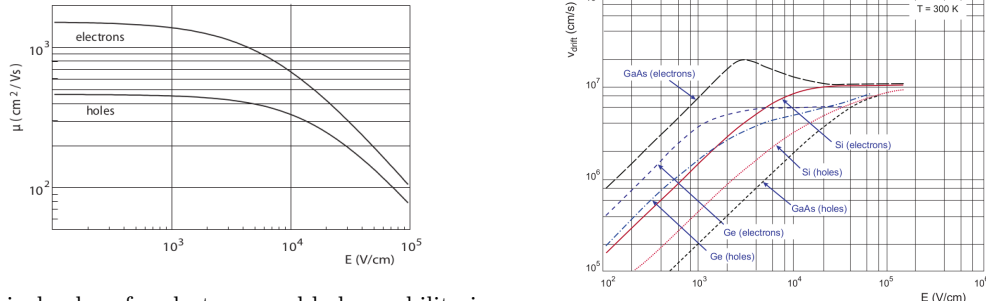
¹²⁵ The average energy needed to create a pair at 300 K in silicon is $w_i = 3.65$ eV, that is more
¹²⁶ than the mean ionization energy because of the interactions with phonon, since for a minimum
¹²⁷ ionizing particle (MIP) the most probable value (MPV) of charge released in the semiconductor is
¹²⁸ 0.28 keV/ μ m, hence the number of electrons-vacuum pairs is:

$$\langle \frac{dE}{dx} \rangle \frac{1}{w_i} \sim 80 \text{ e}/\text{h} \sim \frac{1.28 \cdot 10^{-2} fC}{\mu m} \quad (2.3)$$

¹²⁹ CON UN'INCERTEZZA CHE È RADICE DI N; ED EVENTUALEMTE SI AGGIUNGE IL
¹³⁰ FATTORE DI FANO NEL CASO DI ASSORBIMENTO TOTALE. IL FATTORE DI FANO È
¹³¹ 0.115 NEL SILICIO. ecc

¹³² It is fundamental that pairs e/h are produced in the depleted region of the semiconductor where
¹³³ the probability of recombination with charge carriers is low to avoid loss of signals. Pixel detectors

¹Even if in principle both the electrode can be used to read a signal, for pixel detectors, where the number of channel and the complexity of readout are high, only one is actually used. In strip and pad detectors, instead, is more common a dual-side readout



(a) Typical values for electrons and holes mobility in silicon at room temperature are $\mu_n \sim 1450 \text{ cm}^2/\text{Vs}$, $\mu_h = 500 \text{ cm}^2/\text{Vs}$
(b) Drift velocity at room temperature in different semiconductors

134 are then commonly reverse biased: a positive bias is given to the n electrode and a negative to the
135 p to grow the depletion zone in the epitaxial layer below the electrode. The width of the depletion
136 region is related with the external bias V_{ext} , the resistivity ρ and also with the dopant:

$$d_n \sim 0.55 \sqrt{\frac{\rho}{\Omega cm}} \frac{V_{ext}}{V} \mu m \quad (2.4)$$

138

$$d_p \sim 0.32 \sqrt{\frac{\rho}{\Omega cm}} \frac{V_{ext}}{V} \mu m \quad (2.5)$$

139

140 For that reason high resistivity wafers ($100 \Omega cm - k\Omega cm$) are typically preferred because they
141 allow bigger depletion zone with smaller voltage bias. Metto il disegno "standard" di una giunzione

142 2.2 CCDs

143 descrivi come sono fatte e come funziona il readout Tens of ms due to the need to transfer the
144 charge signals pixel by pixel through a single output circuit For photon imaging the need of high
145 assorbtion efficiency, per cui usi materiali con alto Z

146 2.3 Hybrid pixels

147 METTI IN EVIDENZAZ CHE PUOI FARE UN READOUT CON TECNOLOGIA CMOS. Metti
148 in evidenza che sono più veloci Hybrid pixels are made of two parts (fig. 2.2a), the sensor and the
149 electronics: for each pixel these two parts are welded together through microconnection (bump
150 bond).

151 They provide a practical system where readout and sensor can be optimized separately, although
152 the testing is less easy-to-do since the sensor and the R/O must be connected together before.

153 In addition, the particular and sophisticated procedure to bond sensor and ASIC (application spe-
154 cific integrated circuit) makes them difficult to produce, delicate, especially when exposed to high
155 levels of radiation, and also expensive.

156 A critical parameter for accelerator experiments is the material budget, which represents the main
157 limit factor for momentum measurement resolution in a magnetic field; since hybrid pixels are
158 thicker (\sim hundreds of μm) than monolithic ones (even less than $100 \mu m$), using the latter the
159 material budget can be down by a third: typical value for hybrid pixels is $1.5 \% X_0$ per layer,
160 while for monolithic $0.5 \% X_0$.

161 Among other disadvantages of hybrid pixels there is the bigger power consumption that implies,
162 by the way, a bigger cooling system leading in turn to an increase in material too.

163 DEPFET are the first attempt towards the integration of the front end (FE) on the sensor bulk:
164 they are typically mounted on a hybrid structure but they also integrate the first amplification
165 stage.

166 Each pixel implements a MOSFET (metal-oxide-semiconductor field-effect transistor) transistor
167 (a p-channel in fig. 2.2b): an hole current flows from source to drain which is controlled by the
168 external gate and the internal gate together. The internal gate is made by a deep $n+$ implant

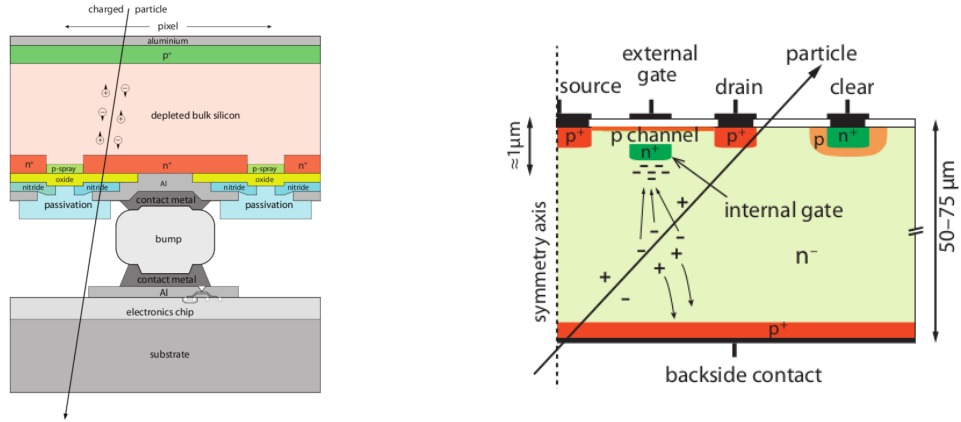


Figure 2.2: Concept cross-section of hybrid pixel (a) and of a DEPFET (b)

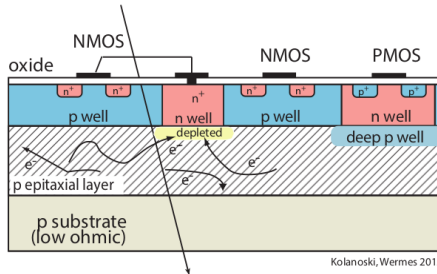


Figure 2.3: Concept cross-section of CMOS MPAS pixel

170 towards which electrons drift after being created in the depletion region (to know how the signal
 171 is created in a pixel detector look at appendix A); the accumulation of electrons in the region
 172 underneath the n implant changes the gate potential and controls the transistor current.
 173 DEPFET typically have a good S/N ratio: this is principally due the amplification on-pixel and
 174 the large depletion region. But, since they need to be connected with ASIC the limiting factor still
 175 is the material budget.

176 2.4 CMOS MAPS and DMPAS

177 With respect to CCDs, the radiation tolerance could be greatly increased by sensing the signal
 178 charge within its own pixel, instead of transporting it over thousands of pixels. The readout
 179 speed could also be dramatically increased by in-pixel amplitude discrimination, followed by sparse
 180 readout of only the hit pixels Monolithic active pixels accommodate on the same wafer both the
 181 sensor and the front end electronics, with the second one implanted on top within a depth of about
 182 1 μm below the surface.

183 MAPS have been first proposed and realized in the 1990s and their usage has been enabled by the
 184 development of the electronic sector which guarantees the decrease in CMOS transistors dimension
 185 at least every two years, as stated by the Moore's law².

186 As a matter of fact the dimension of components, their organization on the pixel area and logic
 187 density are important issues for the design and for the layout; typically different decisions are taken
 188 for different purposes.

189 Monolithic active pixel can be distinguished between two main categories: MAPS and depleted
 190 MAPS (DMPAS).

191 MAPS (figure 2.3) have typically an epitaxial layer in range 1 μm to 20 μm and because they
 192 are not depleted, the charge is mainly collected by diffusion rather than by drift. This makes the
 193 path of charges created in the bulk longer than usual, therefore they are slow (of order of 100 ns)
 194 and the collection could be partial especially after the irradiation of the detector (look at A for
 195 radiation damages), when the trapping probability become higher.

²Moore's law states that logic density doubles every two years.

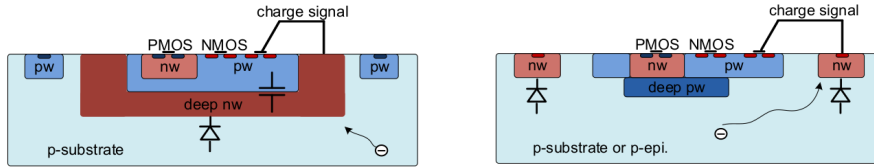


Figure 2.4: Concept cross-section with large and small fill factor

196 In figure 2.3 is shown as example of CMOS MAPS: the sensor in the scheme implements an n well
 197 as collection diode; to avoid the others n wells (which contain PMOS transistor) of the electronic
 198 circuit would compete in charge collection and to shield the CMOS circuit from the substrate,
 199 additionally underlying deep p well are needed. DMAPS are instead MAPS depleted with d
 200 typically in $\sim 25 \mu\text{m}$ to $150 \mu\text{m}$ (eq. 2.1) which extends from the diode to the deep p-well, and
 201 sometimes also to the backside (in this case if one wants to collect the signal also on this electrode,
 202 additional process must be done).

203 2.4.1 DMAPS: large and small fill factor

204 There are two different sensor-design approaches (figure 2.4) to DMAPS:

- 205 • large fill factor: a large collection electrode that is a large deep n-well and that host the
 206 embedded electronics
- 207 • small fill factor: a small n-well is used as charge collection node

208 To implement a uniform and stronger electric field, DMAPS often uses large electrode design that
 209 requires multiple wells (typically four including deep n and p wells); this layout adds on to the
 210 standard terms of the total capacity of the sensor a new term (fig. 2.5), that contributes to the
 211 total amplifier input capacity. In addition to the capacity between pixels (C_{pp}) and between the
 212 pixel and the backside (C_b), a non-negligible contribution comes from the capacities between wells
 213 (C_{WW} and C_{SW}) needed to shield the embedded electronics. These capacities affect the thermal
 214 and 1/f noise of the charge amplifier and the τ_{CSA} too:

$$209 \quad ENC_{thermal}^2 \propto \frac{4}{3} \frac{kT}{g_m} \frac{C_D^2}{\tau_{sh}} \quad (2.6) \quad \tau_{CSA} \propto \frac{1}{g_m} \frac{C_D}{C_f} \quad (2.7)$$

216 where g_m is the transconductance, τ_{sh} is the shaping time.
 217 Among the disadvantages coming from this large input capacity could be the coupling between
 218 the sensor and the electronics resulting in cross talk: noise induced by a signal on neighbouring
 219 electrodes; indeed, since digital switching in the FE electronics do a lot of oscillations, this prob-
 lem is especially connected with the intra wells capacities. So, larger charge collection electrode

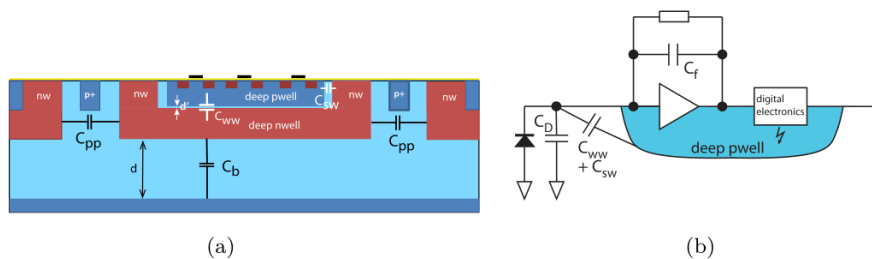


Figure 2.5: C_{pp} , C_b , C_{WW} , C_{SW}

220 sensors provide a uniform electric field in the bulk that results in short drift path and so in good
 221 collection properties, especially after irradiation, when trapping probability can become an issue.
 222 The drawback of a large fill-factor is the large capacity ($\sim 100 \text{ fF}$): this contributes to the noise
 223 and to a speed penalty and to a larger possibility of cross talk.

	small fill factor	large fill factor
small sensor C	✓ (< 5 fF)	✗ (~ 100 200 fF)
low noise	✓	✗
low cross talk	✓	✗
velocity performances	✓	✗ (~100 ns)
short drift paths	✗	✓
radiation hard	✗	✓

Table 2.1: Small and large fill factor DMAPS characteristics

225 The small fill-factor variant, instead, benefits from a small capacity (5 fF to 20 fF), but suffers
 226 from a not uniform electric field and from all the issue related to that. **Ho già detto prima parlando
 227 dei MAPS, devo ripetere qui?**

228 As we'll see these two different types of sensor require different amplifier: the large electrode one is
 229 coupled with the charge sensitive amplifier, while the small one with voltage amplifier (sec 2.5.1).

230 2.4.2 A modified sensor

231 A process modification developed by CERN in collaboration with the foundries has become the
 232 standard solution to combine the characteristics of a small fill factor sensor (small input amplifier
 233 capacity) and of large fill factor sensor (uniform electric field) is the one carried out for ALICE
 234 upgrade about ten years [1].

235 A compromise between the two sensors could also be making smaller pixels, but this solution
 236 requires reducing the electronic circuit area, so a completely new pixel layout should be though.
 237 The modification consists in inserting a low dose implant under the electrode and one its advantage
 238 lies in its versatility: both standard and modified sensor are often produced for testing in fact.

239 Before the process modification the depletion region extends below the diode towards the sub-
 240 strate, and it doesn't extend laterally so much even if a high bias is applied to the sensor (fig. 2.6).
 241 After, two distinct pn junctions are built: one between the deep p well and the n^- layer, and the
 242 other between the n^- and the p^- epitaxial layer, extending to the all area of the sensor.

243 Since deep p well and the p-substrate are separated by the depletion region, the two p electrodes
 244 can be biased separately³ and this is beneficial to enhance the vertical electric field component.

245 The doping concentration is a trimmer parameter: it must be high enough to be greater than the
 246 epitaxial layer to prevent the punchthrough between p-well and the substrate, but it must also be
 247 lower enough to allow the depletion without reaching too high bias.

248 2.5 Analog front end

249 After the creation of a signal on the electrode, the signal enters the front end circuit (fig.2.7), ready
 250 to be molded and transmitted out of chip. Low noise amplification, fast hit discrimination and an
 251 efficient, high-speed readout architecture, consuming as low power as possible must be provided
 252 by the readout integrated electronics (ROIC).

253 Let's take a look to the main steps of the analog front end chain: the preamplifier (that actually
 254 often is the only amplification stage) with a reset to the baseline mechanism and a leakage current
 255 compensation, a shaper (a band-pass filter) and finally a discriminator. The whole chain must be
 256 optimized and tuned to improve the S/N ratio: it is very important both not to have a large noise
 257 before the amplification stage in order to not multiply that noise, and chose a reasonable threshold
 258 of the discriminator to cut noise-hits much as possible.

259 2.5.1 Preamplifier

260 Even if circuits on the silicon crystal are only constructed by CMOS, a preamplifier can be modeled
 261 as an operational amplifier (OpAmp) where the gain is determined by the input and feedback

³This is true in general, but it can be denied if other doping characteristics are implemented, and we'll see that this is the case of TJ-Monopix1

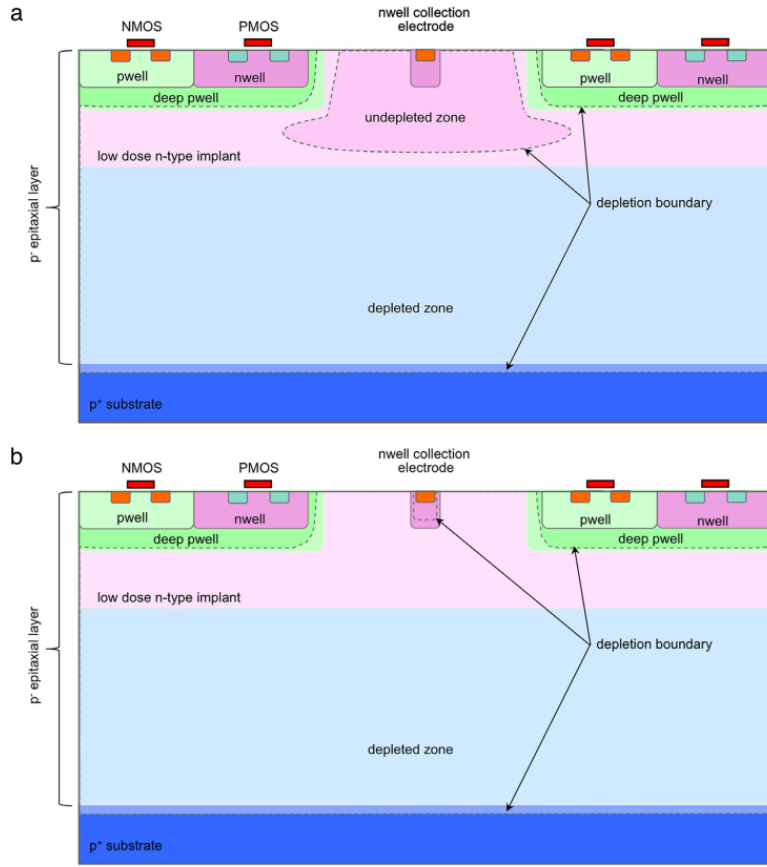


Figure 2.6: A modified process for ALICE tracker detector: a low dose n implant is used to create a planar junction. In (a) the depletion is partial, while in (b) the pixel is fully depleted.

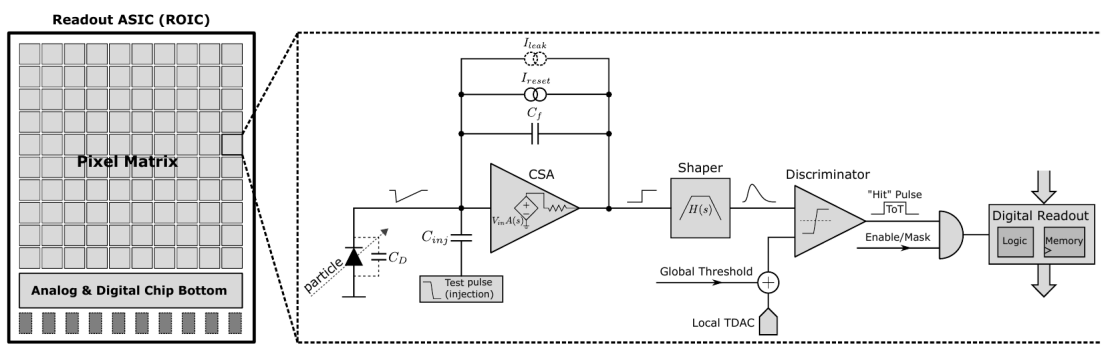


Figure 2.7: Readout FE scheme: in this example the preamplifier is a charge sensitive one (CSA) but changing the capacitive feedback into a resistive one, this can be converted in a voltage or current amplifier.

262 impedance (first step in figure 2.7):

$$G = \frac{v_{out}}{v_{in}} = \frac{Z_f}{Z_{in}} \quad (2.8)$$

263 Depending on whether a capacity or a resistance is used as feedback, respectively a charge or a
 264 voltage amplifier is used: if the voltage input signal is large enough and have a sharp rise time, the
 265 voltage sensitive preamplifier is preferred. Consequently, this flavor doesn't suit to large fill factor
 266 MAPS whose signal is already enough high: $v_{in} = Q/C_D \approx 3\text{fC}/100\text{ pF} = 0.03\text{ mV}$, but it's fine
 267 for the small fill factor ones: $v_{in} = Q/C_D \approx 3\text{fC}/3\text{ pF} = 1\text{ mV}$.

268 In the case of a resistor feedback, if the signal duration time is longer than the discharge time
 269 ($\tau = R_S C_D$) of the detector the system works as current amplifier, as the signal is immediately
 270 trasmit to the amplifier; in the complementary case (signal duration longer than the discharge
 271 time) the system integrates the current on the C_D and operates as a voltage amplifier.

272 2.6 Readout logic

273 Readout logic includes the part of the circuit which takes the FE output signal, processes it and
 274 then transmit it out of pixel and/or out of chip; depending on the situation of usage different
 275 readout characteristics must be provided.

276 To store the analogical information (i.e. charge collected, evolution of signal in time, ...) big buffers
 277 and a large bandwidth are needed; the problem that doesn't occur, or better occur only with really
 278 high rate, if one wants record only digital data (if one pixel is hit 1 is recorded, and if not 0 is
 279 recorded).

280 A common compromise often made is to save the time over threshold (ToT) of the pulse in clock
 281 cycle counts; this needs of relatively coarse requirement as ToT could be trimmer to be a dozen
 282 bits but, being correlated and hopefully being linear with the deposited charge by the impinging
 283 particle in the detector, it provides a sufficient information. The ToT digitalization usually takes
 284 advantage of the distribution of a clock (namely BCID, bunch crossing identification) on the pixels'
 285 matrix. The required timing precision is at least around 25 ns, that corresponds to the period of
 286 bunch collisions at LHC; for such reason a reasonable BCID-clock frequency for pixels detector is
 287 40 MHz.

288 Leading and trailing edges' timestamp of the pulse are saved on pixel within a RAM until they
 289 have been read, and then the ToT is obtained from their difference.

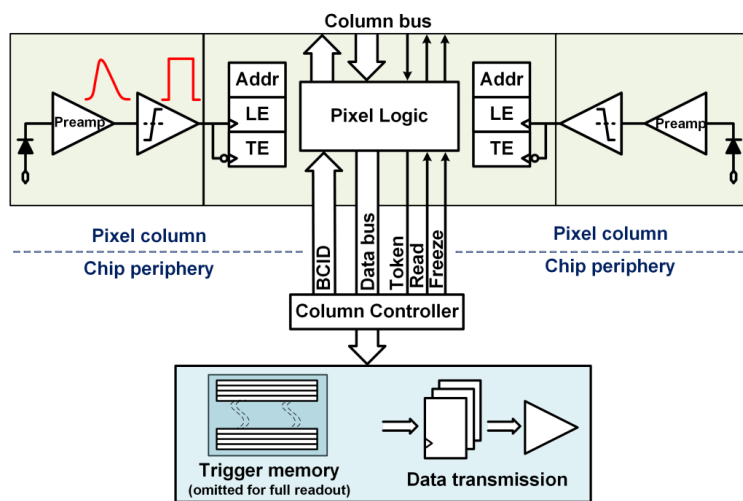


Figure 2.8: Column drain R/O scheme where ToT is saved

289 Moreover, the readout architecture can be full, if every hit is read, or triggered, if a trigger
 290 system decides if the hit must be store or not. On one hand the triggered-readout needs buffers
 291 and storage memories, on the other the full readout, because there is no need to store hit data on
 292 chip, needs an high enough bandwidth.

294 A triggered readout is fundamental in accelerator experiments where the quantity of data to store
 295 is too large to be handled, and some selections have to be applied by the trigger: to give an order

296 of growth, at LHC more than 100 TBit/s of data are produced, but the storage limit is about 100
 297 MBit/s [2] (pag. 797).

298 Typically the trigger signal is processed in a few μs , so the pixel gets it only after a hundred clock
 299 cycles from the hit arrival time: the buffer depth must then handle the higher trigger latency.

300 After having taken out the data from the pixel, it has to be transmitted to the end of column
 301 (EoC) where a serializer deliver it out of chip, typically to an FPGA.

302 There are several ways of transmitting data from pixel to the end of column: one of the most
 303 famous is the column-drain read out, developed for CMS and ATLAS experiments [3]. All the
 304 pixels in a double-column share a data bus and only one pixel at a time, according to a priority
 305 chain, can be read. The reading order circuit is implemented by shift register (SR): when a hit
 306 arrives, the corresponding data, which can be made of timestamp and ToT, is temporarily stored
 307 on a RAM until the SH does not allow the access to memory by data bus.

308 Even if many readout architectures are based the column-drain one, it doesn't suit for large size
 309 matrices. The problem is that increasing the pixels on a column would also raise the number of
 310 pixels in the priority chain and that would result in a slowdown of the readout.

311 If there isn't any storage memory, the double-column behaves as a single server queue and the
 312 probability for a pixel of waiting a time T greater than t , with an input hit rate on the column μ
 313 and an output bandwidth B_W is [4]:

$$P(T > t) = \frac{\mu}{B_W} e^{-(B_W - \mu)t} \quad (2.9)$$

314 To avoid hit loss (let's neglect the contribution to the inefficiency of the dead time τ due to the
 315 AFE), for example imposing $P_T > t \sim 0.001$, one obtains $(B_W - \mu) t_t \sim 6$, where t_t is the time
 316 needed to transfer the hit; since t_t is small, one must have $B_W \gg \mu$, that means a high bandwidth
 [4].

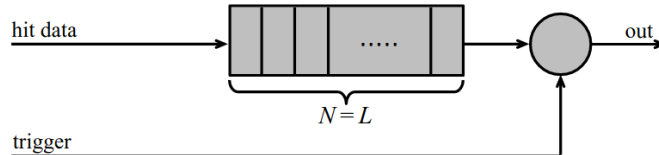


Figure 2.9: Block diagram of a pipeline buffer: N is the dimension of memory buffer and L is the trigger latency expressed in BCID cycles

317 Actually the previous one is an approximation since each pixel sees a different bandwidth de-
 318 pending on the position on the queue: the first one sees a full bandwidth, but the next sees a
 319 smaller one because occasionally it can be blocked by the previous pixel. Then the bandwidth seen
 320 by the pixel i is $B_i = B - \sum_j \mu_j$, where μ_j is the hit rate of the j th pixel.

321 The efficiency requirement on the bandwidth and the hit rate becomes: $B_{W,i} > \mu_i$, where the
 322 index i means the constraint is for a single pixel; if all the N pixels on a column have the same
 323 rate $\mu = N\mu_i$, the condition reduces to $B_W > \mu$. The bandwidth must be chosen such that the
 324 mean time between hits of the last pixel in the readout chain is bigger than that.

325 In order to reduce the bandwidth a readout with zero suppression on pixel is typically employed;
 326 this means that only information from channels where the signal exceeds the discriminator thresh-
 327 old are stored. Qualcosa sulla zero suppression? La metto qui questa affermazione?

328 If instead there is a local storage until a trigger signal arrives, the input rate to column bus
 329 μ' is reduced compared to the hit rate μ as: $\mu' = \mu \times r \times t$, where r is the trigger rate and t is
 330 the bunch crossing period. In this situation there is a more relaxed constraint on the bandwidth,
 331 but the limiting factor is the buffer depth: the amount of memory designed depends both on the
 332 expected rate μ and on the trigger latency t as $\propto \mu \times t$, that means that the higher the trigger
 333 latency and the lower the hit rate to cope with.

334 In order to have an efficient usage of memory on pixels' area it's convenient grouping pixels
 335 into regions with shared storage. Let's compare two different situations: in the first one a buffer
 336 is located on each pixel area, while in the second one a core of four pixels share a common buffer
 337 (this architecture is commonly called FE-I4).

338 Consider a 50 kHz single pixel hits rate and a trigger latency of 5 μs , the probability of losing

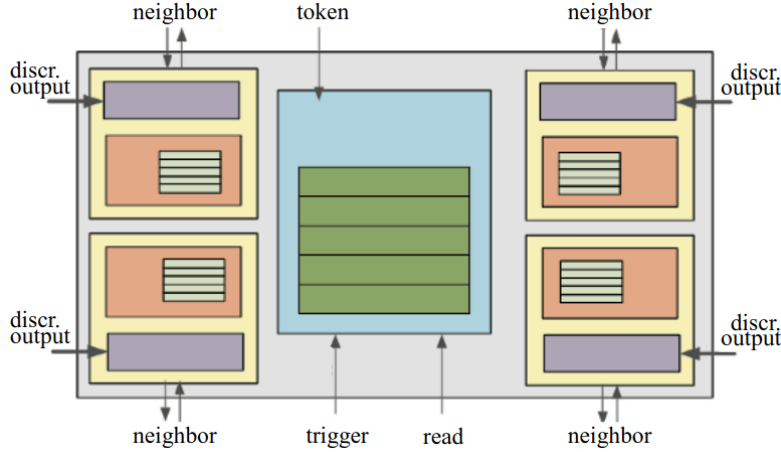


Figure 2.10: Block diagram of the FE-I4 R/O. Read and memory management section is highlighted in light blue; latency counters and trigger management section are highlighted in green; hit processing blocks are highlighted in purple; ToT counters and ToT management units are highlighted in orange

³⁴⁰ hits is:

$$P(N > 1|\nu) = 1 - P(N = 0|\nu) - P(N = 1|\nu) = 1 - e^{-\nu}(1 + \nu) \approx 2.6\% \quad (2.10)$$

³⁴¹ where I have assumed a Poissonian distribution with mean $\nu = 0.25$ to describe the counts N.

³⁴² To get an efficiency ϵ greater than 99.9 % a 3 hit depth buffer is needed:

$$P(N > 3|\nu) = 1 - \sum_{i=0}^3 P(N = i|\nu) < 0.1\% \quad (2.11)$$

³⁴³ Considering the second situation: if the average single pixel rate is still 50 kHz, grouping four pixels
³⁴⁴ the mean number of hits per trigger latency is $\nu = 0.25 \times 4 = 1$. To get an efficiency of 99.9% (eq.
³⁴⁵ 2.11) a buffer depth of 5 hits in the four-pixels region, instead of 3 per pixels, is needed.

³⁴⁶ **Chapter 3**

³⁴⁷ **Use of pixel detectors**

³⁴⁸ There always was a tight relation between the development of cameras and pixel detectors since
³⁴⁹ 1969, when the idea of CCDs, thanks to whom Boyle and Smith were awarded the Nobel Prize in
³⁵⁰ Physics in 2009, revolutionized photography allowing light to be captured electronically instead of
³⁵¹ on film. Even though the CMOS technology was already known when CCDs spread, the costs of
³⁵² productions were too high to allow the diffusion of these sensors for which needed to wait until
³⁵³ 1990s. From that period on, the fast diffusion of CMOS was mainly due to the less cost than
³⁵⁴ CCD, and the less power required for supply. Nowadays CCDs are still preferred over MAPS in
³⁵⁵ astronomy, where the astronomical sources' rate are low enough to cope with tens of ms for the
³⁵⁶ readout.

³⁵⁷ The principal use cases of pixel detectors are particle tracking and imaging: in the former case
³⁵⁸ individual charged particles have to be identified, in the latter instead an image is obtained by
³⁵⁹ the usually un-triggered accumulation of the impinging radiation. Also the demands on detectors
³⁶⁰ performance depends on their usage, in particular tracking requires high spatial resolution, fast
³⁶¹ readout and radiation hardness.

³⁶² **3.1 Tracking in HEP**

³⁶³ At first the physics world overlooked the CCDs, and all pixel in general, as against the gaseous
³⁶⁴ detector for tracking: there was no need to replace these ones which had a sufficient good resolution
³⁶⁵ ($100\text{ }\mu\text{m}$). Since 1974, with the measurement of the invariant mass of the **j psi** and the affirmation
³⁶⁶ of the quark model, all experiments start to look for better spatial resolutions in order to achieve
³⁶⁷ the possibility of reconstructing short lived particle.

³⁶⁸ Historically, the first pixel detector employed in particle physics was a CCD: it was installed in
³⁶⁹ the spectrometer at the CERN's Super Proton Synchrotron (SPS) by the ACCMOR Collaboration
³⁷⁰ (Amsterdam, CERN, Cracow, Munich, Oxford, RAL) at mid 1980s, with the purpose of studying
³⁷¹ the recently-discovered charm particles. The second famous usage of CCDs took place at SLAC
³⁷² in the Large Detector (SLD) during the two years 1996-98. **Cosa vedono di così importante da**
³⁷³ **dire che servono i pixel detector?** From that period on particle tracking in experiments have been
³⁷⁴ transformed radically: it was mandatory for HEP experiments to build an inner vertex detector.
³⁷⁵ In 1991, the more demanding environments led to the development of hybrid pixel detectors:
³⁷⁶ a dedicated collaboration, RD19, was established at CERN with the specific goal to define a
³⁷⁷ semiconductor micropattern detector with an incorporated signal processing at a microscopic level.
³⁷⁸ In those years a wide set of prototypes of hybrid pixel has been manufactured; among the greatest
³⁷⁹ productions a mention goes to the huge ATLAS and CMS vertex detectors. From the middle of
³⁸⁰ 2013 a second collaboration, RD 53, has been established with the new goal to find a pixel detector
³⁸¹ suitable for phase II future upgrades of those experiments. Even if the collaboration is specifically
³⁸² focused on design of hybrid pixel readout chips (aiming to 65 nm technique so that the electronics
³⁸³ fits within the pixel area), also other options have been taken in account and many test have been
³⁸⁴ done on MAPS for example. Requirements imposed by HL-LHC will become tighter in time: for
³⁸⁵ example, a dose and radiation of 5 Mrad and 1016 NIEL are expected after 5 years of operation.
³⁸⁶ Time resolution, material budget and power consumption are also issues for the upgrade: a time
³⁸⁷ resolution better than 25 ns for a bunch crossing frequency of 40 MHz, a material budget lower
³⁸⁸ than 2% and a power consumption lower than 500 mW/cm^2 are required.

389 Amidst the solutions proposed 3D silicon detector, invented by Sherwood Parker in 1995, and
390 MAPS are the most promising. In 3D sensors the electrode is a narrow column of n-type implanted
391 vertically across the bulk instead of being implanted on the wafer's surface. The charge produced
392 by the impinging particle is then drifted transversally within the pixel, and, as the mean path
393 between two electrode can be sufficient low, the trap probability is not an issue. 3D pixels have
394 been already proved in ATLAS tracker [quando?](#). Even if 3D detector are adequately radiation hard,
395 MAPS architecture looked very promising from the beginning: they overcome both the CCDs long
396 reading time and the hybrid problems (I have already explained in section ?? the benefits of
397 MAPS). Experiments such as ALICE at LHC and STAR at RHIC have already introduced the
398 CMOS MAPS technology in their detectors. ALICE Tracking System (ITS2), upgraded during the
399 LHC long shut down in 2019-20, was the first large-area ($\sim 10 \text{ m}^2$ covered by 2.5 Gpixels) silicon
400 vertex detector based on CMOS MAPS.

401 3.1.1 Hybrid pixels at LHC and at SuperKEKB

402 ATLAS

403 With CMS, ATLAS is one of two general-purpose detectors at the LHC and has the largest volume
404 detector ever constructed for a particle collider (46 m long and 25 m in diameter). The Inner
405 Detector consists of three different systems all immersed in a magnetic field parallel to the beam
406 axis whose main components are: the pixel, the micro-strips and transition radiation trackers.
407 Concerning the pixel detector, 92 million pixels are divided in 4 barrel layers and 3 disks in each
408 end-cap region, covering a total area of 1.9 m^2 and having a 15 kW of power consumption.

409 As stated by the ATLAS collaboration the pixel detector is exposed by an extreme particle
410 flux: "By the end of Run 3¹, the number of particles that will have hit the innermost pixel layers
411 will be comparable to the number it would receive if it were placed only a few kilometres from
412 the Sun during a solar flare". Considering that the particle density will increase even more with
413 HL-LHC, radiation hardness is definitively target to achieve.

414 The most ambitious goal is employ a MAPS-based detector for the inner-layer barrels, and for
415 this reason the RD53 collaboration is performing many test on MAPS prototypes, as Monopix of
416 which I will talk about in section ??.

417 Up to now this possibility will be eventually implemented during the second phase of the HL-
418 LHC era, as at the start of high-luminosity operation the selected option is the hybrid one. The
419 sensor will be bonded with ITkPix, the first full-scale 65 nm hybrid pixel-readout chip developed
420 by the RD53 collaboration. Regarding the sensor, a valueable option is using 3D pixels, which
421 have already proved themselves in ATLAS, for the insertable B layer (IBL).[qualcosa in più sui 3d.](#)
422 The number of pixels will be increased of a factor about 7, passing from 92 milions to 6 billion.

423 CMS

424 [da scrivere](#) 124 million pixels; cylindrical layers roughly at 3cm, 7cm, 11cm and 16cm and disks at
425 either end, and so will be vital in reconstructing the tracks of very short-lived particles. Each of
426 these silicon pixels is 100um by 150um,even with only around 50 microwatts per pixel, the total
427 power output is 7.5kW-

428 LHCb

429 LHCb is a dedicated heavy-flavour physics experiment that exploits pp interactions at 14 TeV at
430 LHC. It was the last experiment to upgrade the vertex detector, the Vertex Locator (VELO),
431 replacing the silicon-strip with pixels in May 2022. As the instantaneous luminosity in Run3 is
432 increased by a factor $\lesssim 10$, much of the readout electronics and of the trigger system have been
433 developed in order to cope with the large interaction rate. To place the detector as close as possible
434 to the beampipe and reach a better track reconstruction resolution, the VELO has a surprising
435 feature: it can be moved. During the injection of LHC protons it is parket at 3 cm from the beams
436 and only when the stability is reach it is brought at ~ 5 mm. Radiation hardness as well as readout
437 speed are then a priority for the detectors: that's why the collaboration opted for a hybrid system.
438 The Velopix is made bonding sensors, each measuring 55×55 micrometers, $200 \mu\text{m}$ -thick to a
439 $200 \mu\text{m}$ -thick ASIC specially developed for LHCb and coming from the Medipix family (sec. ??),

¹Run 3 start in June 2022

440 which can handles hit rates up to 900 MHz per chip. Since the detector is operated under vacuum
441 near the beam pipe, the heat removal is particularly difficult and evaporative CO₂ microchannel
442 cooling are used.

443 **BelleII**

444 The current vertex detector of BelleII, VXD, is made of a pixel detector (PXD), fabricated with
445 2 layers of DEPFET-based pixels, and 4 layers of a double-sided silicon strip detectors (SVD)[5].
446 Due to the small capacitance of the collection node, DEPFET presents a high signal-to-noise ratio
447 (in 30-50) thanks to the low intrinsic noise and to the large signal achieved with the fully depleted
448 bulk: pixels are thinned to 75 μm in the active region, then a MIP is supposed to create a signal of
449 $\sim 6000 \text{ e}^-$, while the typical noise of DEPFET is around 200 e^- . **The ASIC read out is still based
450 on a rolling shutter logic, with an integration time of 20 μs .** In order to reduce the data-storage
451 memory PXD hits are only used to improve spatial resolution of tracks: the SVD informations are
452 used by the High Level Trigger (HLT) to look for regions of interest in the pixel ladders just by
453 extrapolating back the tracks found in the tracker detector, and this method allows to store only
454 data belonging to these areas; the PXD hits are then used in offline track fit to improve the vertex
455 resolution.

456 MAPS have been proposed for the replacement of VXD during the Long Shut Down 2 (LSD2)
457 foreseen around 2026-27; the new vertex detector, VTX, should be made of 5 layers fabricated
458 by the optimized Belle II pixel sensor (OBELIX), a detector based on TJ-Monopix have been
459 selected (look at chapter ??). The main advantages VTX should bring are a obvious improving
460 in the track and vertex resolution (14 μm before upgrade, $\lesssim 10 \mu\text{m}$ expected after upgrade) and a
461 reduction in the X_0 (**da.. a..**), a higher background tolerance because of the smaller sensor than
462 strips dimension and a low bandwidth due to the on-chip sparsification.

463 **3.1.2 First attempts to MAPS**

464 **MIMOSA at EUDET and STAR**

465 MIMOSA [6][7] (standing for Minimum Ionizing MOS Active pixel sensor), designed in 2008,
466 prefigured the architecture of MAPS for coming vertex detector being the first large scale sensor
467 to be employed as detector. MIMOSA-26 equipped the final version of EUDET high resolution
468 beam telescope both at CERN-SPS and at DESY while the MIMOSA-28 devices are used for
469 the first MAPS-based vertex detector at the STAR experiment. MIMOSA-26 is fabricated in a
470 350 nm, and a module features 1152 columns, split into 18 independent groups, and 576 rows, with
471 square pixels having a side of 18.4 μm length; therefore, because of the small dimension, charge
472 sharing is an issue **aggiungi qualcosa**. The readout is done in a rolling shutter mode: the chip is
473 an Active Pixels (APS) and therefore it incorporates the amplification on pixel, while the signal
474 discrimination and zero-suppression logic are placed at the EoC, where is also placed a memory.
475 The chip is an Active Pixels (APS) and therefore it incorporates the amplification on pixel, while
476 the signal discrimination and zero-suppression logic are placed at the EoC: the readout is done in
477 a rolling shutter mode with a frame integration time that can be lowered down to 85 ms, and a
478 memory allowing to store up to six hits is.

479 The EUDET telescope, equipped with six sensor planes, requires highly granular and thin pixel
480 detectors in order to achieve an excellent track resolution (around 2 μm) even at the rather low
481 particle energies of up to 6 GeV. The STAR experiment at the Relativistic Heavy Ion Collide
482 (RHIC) accelerator at the Brookhaven National Laboratory (BNL) is the first to include MAPS
483 in the vertex detector[8]. The main tracking detector in STAR is a TPC with radii 60-190 cm
484 embedded in a 0.5 T solenoidal magnetic field, that provides a pointing resolution of approximately
485 1 mm. The pixel detector, PXL, is a part of a 3-detector system, Heavy Flavor Tracker (HFT), that
486 has been added to the pre-existing STAR apparatus just before the 2014 Run in order to improve
487 the impact parameter resolution and to enable the direct reconstruction of hadronic decays of heavy
488 flavor mesons and baryons. The Heavy Flavor Tracker (HFT) is composed by the Silicon Strip
489 Detector (SSD), the Intermediate Silicon Tracker (IST) and the Pixel Detector (PXL); the first
490 one is placed at 22 cm from the beam pipe and consists of double sided strips with 95 μm inter-strip
491 pitch, the second one, placed at 14 cm, is made of single sided silicon pads with 600 $\mu\text{m} \times 6 \text{ mm}$ pitch
492 and the last one made by two layers is placed at 2.8 cm and 8 cm fabricated with ULTIMATE2 (also
493 known as MIMOSA-28), a successor of MIMOSA-26 sensor, with pitch 20.7 μm and thinned down

494 to 50 μm . An area of 0.16 m^2 are covered by 400 MAPS sensor, corresponding to 356 millions of
 495 pixels divided into array size of 928×960 . Each pixel includes circuitry for readout, amplification,
 496 and Correlated Double Sampling (CDS) for signal extraction and noise subtraction and the frame
 497 integration time is 185.6 μs ; after the subtraction the signal to noise ratio is ~ 30 , with a noise
 498 between 10-12 electrons and a signal of 1000 e^- . Thanks to the HFT system and the PXL, STAR
 499 achieved a track pointing resolution 46 μm for 750 MeV/c kaons, and better than 30 μm for particle
 500 momenta bigger than 1 GeV/c: this performance enabled the study of D-meson production with a
 high significance signal.

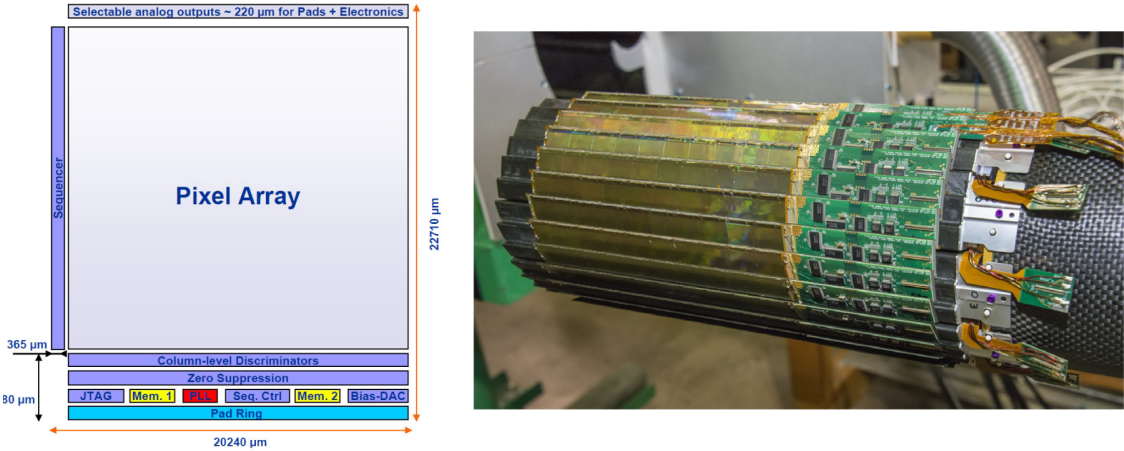


Figure 3.1: (a) The HFT PXL detector; (b) Block-diagram of the ULTIMATE-2 sensor

501

502 ALPIDE at ALICE

503 ALICE (A Large Ion Collider Experiment) is a detector dedicated to heavy-ion physics and to the
 504 study of the condensed phase of the chromodynamics at the LHC. The tracking detector consists of
 505 the Inner Tracking System (ITS), the gaseous Time Projection Chamber (TPC) and the Transition
 506 Radiation Detector (TRD), and all those are embedded in a magnetic field of 0.5 T. The ITS is
 507 made by six layers of detectors, two for each type, from the interaction point outwards: Silicon
 508 Pixel Detector (SPD), Silicon Drift Detector (SDD) and Silicon Strip Detector (SSD). Contrary
 509 to the others LHC experiments, ALICE tracker in placed in a quite different environments: the
 510 expected dose is smaller by two order of magnitude and the rate of interactions is few MHz instead
 511 of 40 MHz, but the number of particles comes out of each interaction is higher (the SPS is invested
 512 by a density of particles of $\sim 100 \text{ cm}^{-2}$). The reconstruction of very complicated events whit a large
 513 number of particle is a challenge, hence to segment and to minimize the amount of material, which
 514 may cause secondary interaction complicating futher the event topology, is considered a viable
 515 strategy. The detector employes the ALPIDE chip, developed by ALICE collaboration, fabricated
 516 in the 180 nm CMOS Imaging Sensor process of TowerJazz, whose design takes full advantage of
 517 process feature which allows full circuitry within the pixel matrix. Thanks to the reduction of the
 518 material budget, ITS2 obtained an amazing improvement both in the position measurement and
 519 in the momentum resolution, improving the efficiency of track reconstruction for particle with very
 520 low transverse momentum (by a factor 6 at $p\text{T} \sim 0.1 \text{ GeV}/c$). Further advancements in CMOS
 521 MAPS technology are being aggressively pursued for the ALICE ITS3 vertex detector upgrades
 522 (foreseen around 2026-27), with the goals of further reducing the sensor thickness and improving
 523 the readout speed of the devices, while keeping power consumption at a minimum.

524 3.2 Other applications

525 Historically for imaging pourpose the CCDs were the favoured device: they can be used as single
 526 photon counter or integrating and collecting the charge released by more impinging particles. The
 527 utilisation in the first case is similar to the tracking one, except that the requirements are less
 528 tight, so much that two noteworthy of microchips originally meant for detectors in particle physics
 529 at the LHC, and later employed in other fields are Medipix and Timepix. They are read-out chips

530 developed by the Medipix Collaborations since early 1990s. For two decades, different Medipix
531 generations have been produced, having a rough correlation with the feature size used: Medipix2
532 (1999) used 250 nm feature size CMOS while Medipix3 (2005) 130 nm. The aim of the fourth col-
533 laboration (2016), instead, is designing pixel read-out chips that prepared for TSV processing and
534 may be tiled on all four sides. **DOVREI METTERE DUE RIGHE SU TSV OPPURE TAGLIARE.**

535 For photons imaging other materials with higher atomic charge than silicon could be prefered,
536 as a high photon absorption efficiency is needed: it was for this reason that Medipix2 was bump
537 bonded to identically segmented sensors of both silicon and GaAs.

538 The applications in scientific imaging vary from astrophysics and medical imaging to more exotic
539 domains as studies of protein dynamics, art authentication and dosimetry. The most important
540 employment of Medipix is as X-ray single photon counting in industrial and medical radiography
541 and in 3D computed tomography. Thanks to a New-Zealand company, the MARS Bioimaging
542 detector has been fabricated, which is capable of resolving the photons energy and produce 3D
543 coloured images. Besides tracking in HEP (I have already cited the use of Timepix3 is in the beam
544 telescope of the LHCb VELO), an important use of Timepix is in dosimetry **Timepix Detector**
545 **for Imaging in Ion Beam Radiotherapy- aggiungi qualche info** A small-Timepix detector with the
546 dimension of a USB can also be found at the International Space Station, where it is exploited for
547 radiation, principally made of heavy-ion, monitoring.

548 3.2.1 Applicability to FLASH radiotherapy

549 A possible new application of pixels detector is dosimetry or beam monitoring of charge particles in
550 high intensity radiography. The radiological treatment is a common method used in 60% of tumors
551 both as palliative care and as treatment. It can be given before, after or during a surgery, (Intra
552 operative radiation therapy-IORT) and many different types of radiations (photons, electrons,
553 protons and ions, which mainly are hydrogen and carbon) can be used to irradiate the affected
554 tissues. Exploiting the ionizing energy loss, that can be parametrized by the Linear Energy
555 Transfer (LET), a biological damage can be delivered to the tissue: while α and β particles are
556 high LET radiations with values in $100 \text{ keV}/\mu\text{m}$ to $200 \text{ keV}/\mu\text{m}$, x-rays and gamma-rays are low
557 LET radiations with values in range $0.2 \text{ keV}/\mu\text{m}$ to $2 \text{ keV}/\mu\text{m}$.

558 If x-ray photons, with energy in 4 MeV to 25 MeV are used, the ionization is caused by the
559 Compton electrons and is more in the superficial layers of the tissue due to the exponential attenu-
560 ation of the beam. The hadrons energy loss, instead, is strongly localized in the last region of the
561 track, that is the Bragg peak. Ion beam enables better focusing of the radiation thereby improves
562 the sparing of the surrounding healthy tissues; on the other hand the delivered dose distribution
563 depends more on the patient's density tissues (e.g. bones, swelling, fat). **Ensuring the target**
564 **coverage is a fundamental objective in radiotherapy and is closely connected to the choice of the**
565 **particles.** Electrons cover the target since they tend to spread out and can cover a field size of a few
566 cm^2 at a distance of a few cm from the source. Instead, the limited size of the beam for protons
567 and photons from ultra high dose rate microbeam radiation therapy (MRT), for which FLASH
568 effect was seen, requires the scanning of target. The radiobiological consequences of scanning both
569 in spatial-fractionation and in prolonged exposure, which might not be sufficient to maintain a
570 high mean dose rate to trigger FLASH effect, need to be explored. To date, the FLASH effect has
571 been most commonly demonstrated using low-energy electron linacs

572 Recently² a promising method for RT at ultra high dose rate (at least 40 Gy/s) and for this
573 reason called FLASH-RT[9], instead of CONV-RT (0.03 Gy/s), came out. This treatment takes
574 advantages of biological differences between tumors and healthy tissues: it is characterized by
575 reducing normal tissue toxicity and maintaining equivalent tumor damage. The response to dose
576 can be described by the survival fraction probability, describing the fraction of surviving cell as a
577 function of the dose:

$$S(D) = S(0) e^{-(\alpha D + \beta D^2)} \quad (3.1)$$

578 where α and β respectively represents the rate of cell killing by single ionizing events and by
579 double hits. Hence, at high doses the density of damages increases and the cells repair becomes
580 more difficult. Even if the FLASH effect is not yet completely understood and the underlying
581 mechanisms are not clear, it looks like there are two different recipes which are involved:

²The first evidences has been observed on mice experiments in 1966 and in 2014 by the group of Favaudon and Vozenin. After this, many test on cats and pigs have been performed, and also there has been a clinical trial on a cutaneous tumor-patient

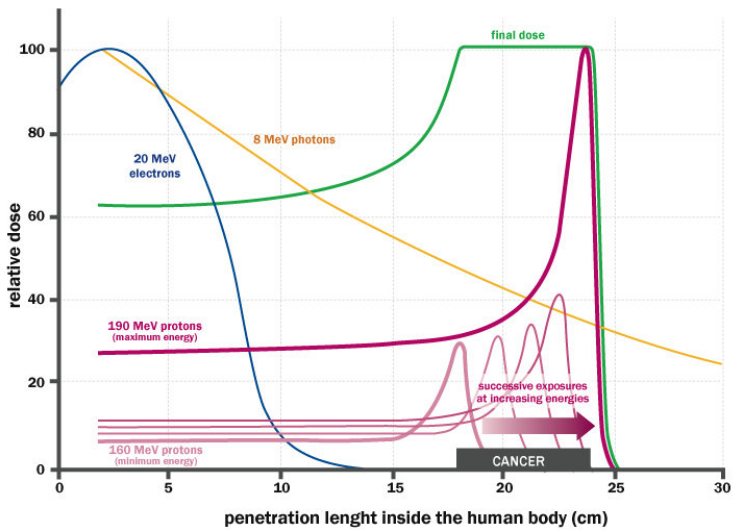


Figure 3.2: The Spread Out Bragg Peak (SOBP) curve (green), which is a constant dose distribution, is obtained from the superposition of many Bragg peak of hadrons with different energy.

	CONV-RT	FLASH-RT
Dose rate	0.03 Gy/s	40 Gy/s
Intra pulse dose rate	100 Gy/s	106 Gy/s
Treatment duration	~minutes	$\lesssim 500$ ms
DDP	0.3 mGy	1 Gy to 10 Gy
Pulse width	3 μ s	~ 2 μ s

Table 3.1: Typical value of treatment parameters

- 582 • **The dose rate:** higher dose rate produce bigger damages (fig. 3.3(a)) since this prevent
583 cells from sparing.
- 584 • **The presence or absence of oxygen:** while hypoxic cells are very resistant to radiation,
585 normal oxygenated cells are highly radiosensitive. This is because if molecules containing O_2
586 break due to the impinging radiation, then the oxygen can build Reactive Oxygen Species
587 (ROS) (fig.3.3(b))

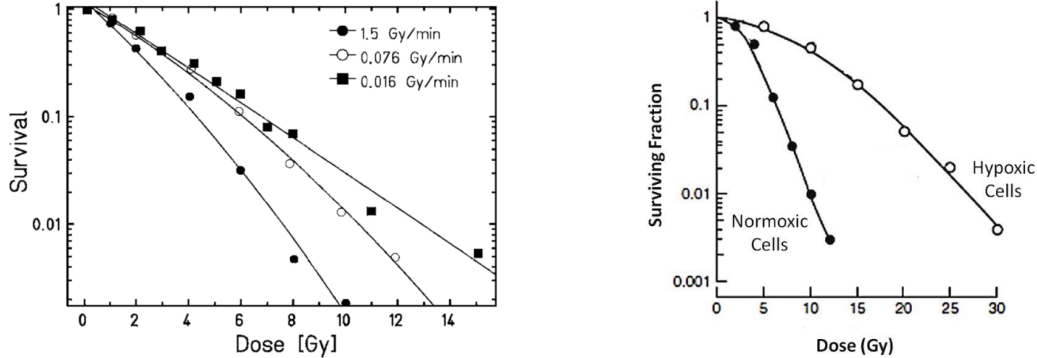


Figure 3.3: (a) Survival curve for different dose rate and (b) for different oxygen cell content

588 The Tumor Control Probability (TCP) and the Normal Tissue Complication (NTC) functions
589 parametrize respectively the efficiency of damaging on the tumor after having released a certain
590 dose and the probability of not affecting the healthy tissues. The intermediate zone between the
591 increase of the TC and of the NTC is called therapeutic window, and the wider it is and the more
592 effective the treatment is.

593 Dosimetric problems

594 Finding dosimeters suitable for online monitoring of the beam at ultra high dose rate is still an
595 open issue since almost all standard online dosimeters show saturation problems. Differently,
596 radiochromic films, which are the standard passive dosimeters, show dose-rate independence up to
597 109 Gy/s. **Cosa sono i radiochromic films and they do not have the same accuracy of other detectors.**
598 The principal detectors for reference dosimetry which provide real-time dose measurement are
599 Ionization Chambers (IC), that show saturation issue at dose per pulse (DDP) two orders of
600 magnitude lower than the ones used for FLASH-RT. **da qui in poi** ICs devono essere calibrate
601 secondo la metrologia , per cui grazie a protocolli di calibrazione e introducendo dei fattori correttivi
602 si riesce a fare una misura di dose. k_{sat} which accounts for the loss of charge collected due to
603 recombination. Doppi problemi sia di saturazione dovuta a ion recombination sia di scariche, must
604 be carefully accounted for: questo doppio effetto è dato dal fatto che, creandosi tante cariche nella
605 camera, che va ad annullare il campo elettrico di drift. Questo ovviamente paralizza le cariche che
606 non driftano più, ma che anzi si ricombinano ed inoltre facilita la formazione di scariche. Per DDP
607 minori di 1 mGy il fattore correttivo è minore al 5%, poi però aumenta substantially.

608 Scintillators have reusable, non-exhaustible scintillation centers. However, the system has a
609 total deadtime given by both the crystal scintillation time and the electronics read-out deadtime.

610 Semiconductors show a nonreversible saturation beyond a threshold around 15 cGy/p. The
611 scintillator used, shows a negligible saturation up to 1 Gy/p, but it increases significantly up to at
612 least 11 Gy/p, and it reaches a cutoff value between 11 and 36 Gy/p.

613 Scintillator dosimeters are widely used in radiotherapy. They are usually operating in counting-
614 mode where each detected signal is processed by read-out electronics. However, the system has a
615 total deadtime given by both the crystal scintillation time and the electronics read-out deadtime
616 When a scintillator dosimeter is used in integrator-mode the signal is integrated over the entire
617 irradiation time. A deadtime, due to the decay time of the scintillating material, is considered on
618 average every N recorded pulses, where N is the number of scintillation centres in the dosimeter.

619 Besides saturation two other requirements for online dosimeters are high temporal and space res-
620 olutions. **Si potrebbe pensare di poter usare i pixel detector as beam monitor che hanno risoluzioni**
621 **spaziali anche inferiori al 10 um e ris temporali -qua dare un valore è più difficile perchè per i**

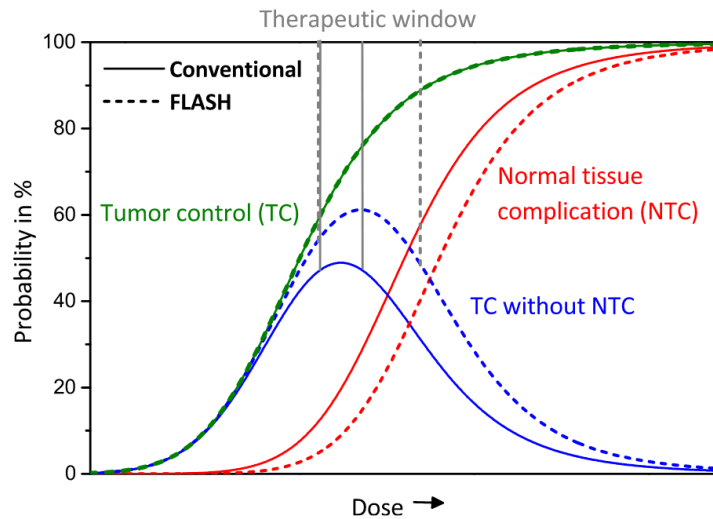


Figure 3.4: Illustration of dependence of TCP, NTCP and therapeutic window on dose, for CONV-RT ad FLASH-RT.

622 maps la risoluzione temporale dipende da l occupancy. Uno dei problemi è però il lungo dead time
 623 introdotto dal lungo tempo di readout (ricorrdiamo che sopportano circa 100 Mhz/cm²).

624

Chapter 4

625

TJ-Monopix1

626 TJ-Monopix1 is a small electrode DMAPS with fast R/O capability, fabricated by TowerJazz
 627 foundry in 180 nm CMOS imaging process. It is part, together with prototypes from other series
 628 such as TJ-MALTA, of the ongoing R&D efforts aimed at developing DMAPS in commercial CMOS
 629 processes, that could cope with the requirements at accelerator experiments. Both TJ-Monopix
 630 and TJ-MALTA series [10], produced with the same technology by TowerJazz (the timeline of the
 631 foundry products is shown in figure 4.1), are small electrode demonstrators and principally differ in
 632 the readout design: while Monopix implements a column-drain R/O, an asynchronous R/O without
 633 any distribution of BCID has been used by TJ-Malta in order to reduce power consumption.



Figure 4.1: Timeline in TowerJazz productions in 180 nm CMOS imaging process

634 Another Monopix series, but in 150 nm CMOS technology, has been produced by LFoundry [11].
 635 The main differences between the LF-Monopix1 and the TJ-Monopix1 (summarized in table 4.2),
 636 lay in the sensor rather than in the readout architecture, as both chips implements a fast column
 637 drain R/O with ToT capability [12][13]. Concerning the sensors, either are based on a p-type
 638 substrate, but with slightly different resistivities; in addition LFoundry pixels are larger, thicker
 639 and have a large fill factor (the very deep n-well covers ~55% of the pixel area). The primary
 640 consequence is that LF-Monopix1 pixels have a higher capacity resulting in higher consumption
 641 and noise. As I discussed in section 2.4.1, the fact that LF-Monopix has a large fill factor electrode
 642 is expected to improve its radiation hardness. Indeed, a comparison of the performance of the
 643 two chips showed that TJ-Monopix suffers a comparatively larger degradation of efficiency after
 644 irradiation, due to the low electric field in the pixel corner; on the other hand, a drawback of the
 645 large fill factor in LF-Monopix is a significant cross-talk.

646 The TJ-Monopix1 chip contains, apart from the pixels matrix, all the required support blocks
 647 used for configuration and testing:

- 648 • the whole matrix contains 224×448 pixels, yielding a total active area approximately equal
 649 to 145 mm^2 over a total area of $1 \times 2 \text{ cm}^2$;
- 650 • at the chip periphery are placed some 7-bit Digital to Analog Converter (DAC), used to
 651 generate the analog bias voltage and current levels and to configure the FE;

	LF-Monopix1	TJ-Monopix1
Resistivity	$>2\text{ k}\Omega\text{cm}$	$>1\text{ k}\Omega\text{cm}$
Pixel size	$50 \times 250\mu\text{m}^2$	$36 \times 40\mu\text{m}^2$
Depth	$100\text{-}750\mu\text{m}$	$25\mu\text{m}$
Capacity	$\sim 400\text{ fF}$	$\sim 3\text{ fF}$
Preamplifier	charge	voltage
Threshold trimming	on pixel (4-bit DAC)	global threshold
ToT	8 bits	6 bits
Consumption	$\sim 300\text{ mW/cm}^2$	$\sim 120\text{ mW/cm}^2$
Threshold	$1500 e^-$	$\sim 270 e^-$
ENC	$100 e^-$	$\sim 30 e^-$

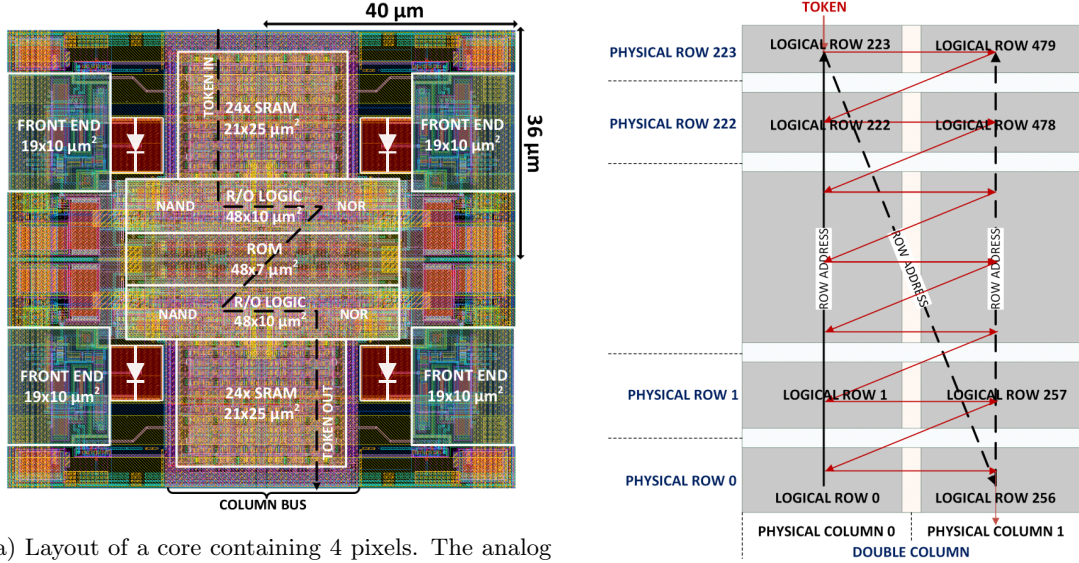
Table 4.1: Main characteristics of Monopix1 produced by TowerJazz and LFoundry [12][13]

- at the EoC is placed a serializer to transferred datas immediately, indeed no trigger memory is implemented in this prototypes;

the matrix power pads are distributed at the sides

- four pixels which have analog output and which can be monitored with an oscilloscope, and therefore used for testing

Pixels are grouped in 2×2 cores (fig. 4.2a): this layout allows to separate the analog and the digital electronics area in order to reduce the possible interference between the two parts. In addition it simplifies the routing of data as pixels on double column share the same column-bus to EoC. Therefore pixels can be addressed through the physical column/row or through the logical column/row, as shown in fig. 4.2b: in figure is also highlighted the token propagation path, whose I will discuss later.



(a) Layout of a core containing 4 pixels. The analog FE and the digital part are separated in order to reduce cross-talk be

(b)

4.1 The sensor

As already anticipated, TJ-Monopix1 has a p-type epitaxial layer and a n doped small collection electrode ($2\mu\text{m}$ in diameter); to avoid the n-wells housing the PMOS transistors competing for the charge collection, a deep p-well substrate, common to all the pixel FE area, is used. TJ-Monopix1 adopts the modification described in section 2.4.2 that allows to achieve a planar depletion region

Parameter	Value
Matrix size	$1 \times 2 \text{ cm}^2$
Pixel size	$36 \times 40 \mu\text{m}^2$
Depth	$25 \mu\text{m}$
Electrode size	$2 \mu\text{m}$
BCID	40 MHz
ToT-bit	6
Power consumption	$\sim 120 \text{ mW/cm}^2$

Table 4.2

near the electrode applying a relatively small reverse bias voltage. This modification improves the efficiency of the detector, especially after irradiation, however a simulation of the electric field in the sensor, made with the software TCAD (Technology Computer Aided Design), shows that a nonuniform field is still produced in the lateral regions of the pixel compromising the efficiency at the corner. Two variations to the process have been proposed in order to further enhance the transversal component of electric field at the pixel borders: on a sample of chip, which includes the one in Pisa, a portion of low dose implant has been removed, creating a step discontinuity in the deep p-well corner (fig. 4.3); the second solution proposed[MOUSTAKAS THESYS, PAG 58] consists in adding an extra deep p-well near the pixel edge. A side effect of the alteration in the low dose implant is that the separation between the deep p-well and the p-substrate becomes weak to the point that they cannot be biased separately to prevent the punchthrough.

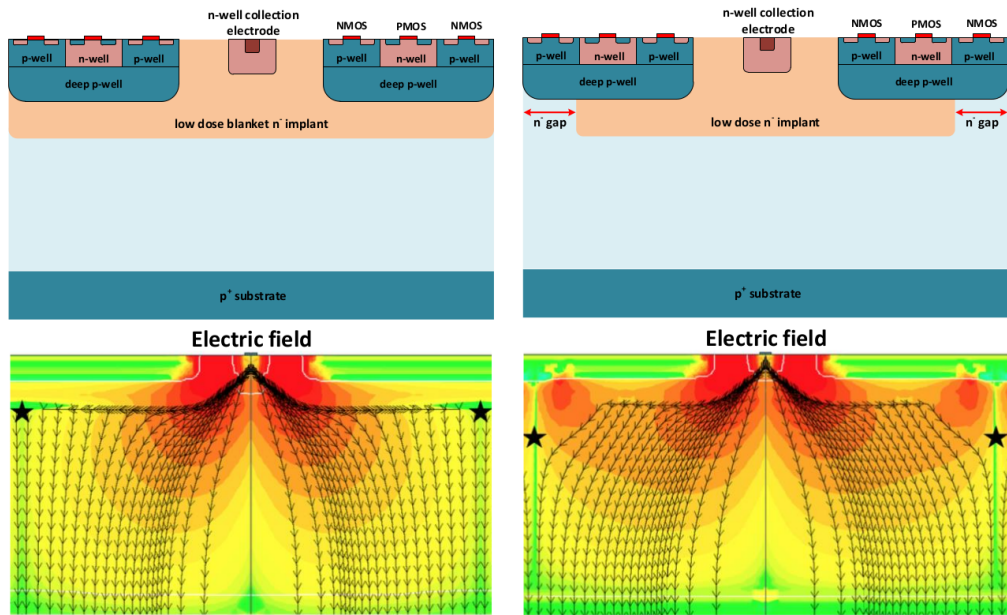


Figure 4.3: (a) The cross-section of a monolithic pixel in the TJ-Monopix with modified process; additionally in (b) a gap in the low dose implant is created to improve the collection of charge due to a bigger lateral component of the electric field. this point in figure is indicated by a star . transversal component of the electric field drops at the pixel corner

Moreover, to investigate the charge collection properties, pixels within the matrix are split between bottom top half and bottom half and feature a variation in the coverage of the deep p-well: the electronics area can be fully covered or not. In particular the pixels belonging to rows from 0 to 111 are fully covered (FDPW) and pixels belonging to rows from 112 to 223 have a reduced p-well (RDPW), resulting in an enhancement of the lateral component of the electric field.

684 4.2 Front end

685 The matrix is split in four sections, each one corresponding to a different flavor of the FE. The
 686 four variation have been implemented in order to test the data-bus readout circuits and the input
 687 reset modes.

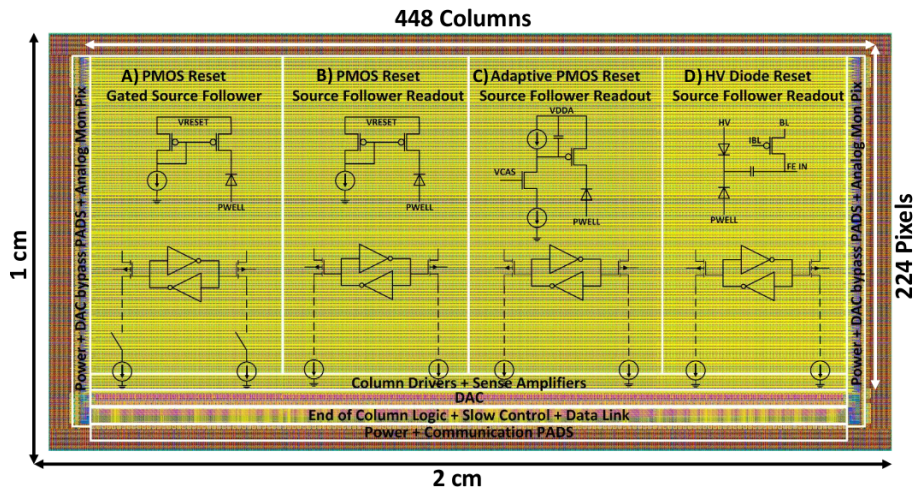


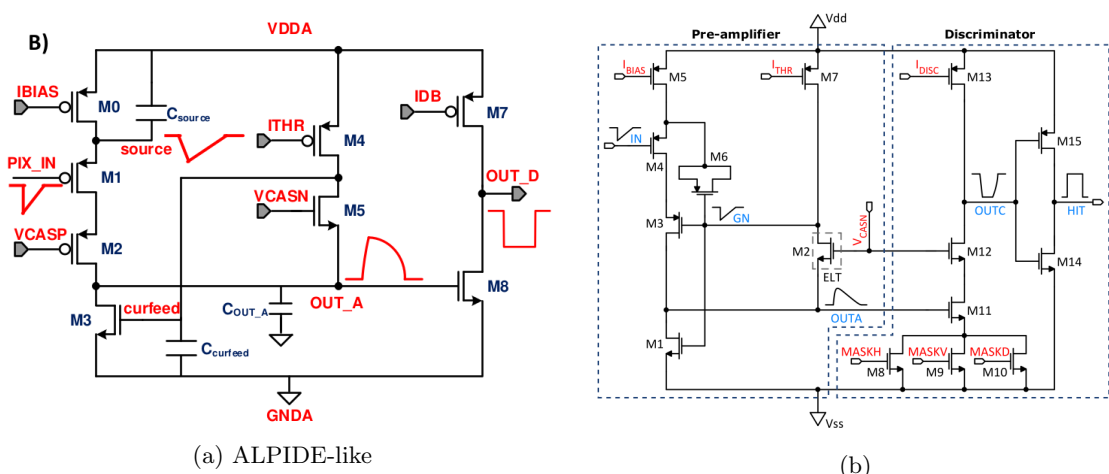
Figure 4.4

687 All the flavors implement a source-follower double-column bus readout: the standard variation
 688 is the flavor B, that features a PMOS input reset (referred as "PMOS reset"). Flavor A is identical
 689 to flavor B except for the realization of the source follower (it is a gated one) that aim to reduce
 690 the power consumption. cosa significa? C instead implements a novel leakage compensation circuit.
 691 Moreover the collection electrode in flavors A, B, C is DC-coupled to the front-end input, while
 692 in D is AC-coupled, providing to apply a high bias voltage; for this reason flavor D is called "HV
 693 flavor".

694 Principio generale: R resistenza di reset deve essere abbastanza grande in modo da far sì che
 695 il ritorno allo zero è abbastanza lento (non devi "interferire" con la tot slope e non deve essere
 696 più corto del tempo del preamplificatore, sennò hai perdita di segnale). Baseline reset: all'input
 697 solitamente hai un PMOSS o un diodo; R reset

699 4.2.1 ALPIDE-like

700 ALPIDE chips, developed by the ALICE collaboration, implemented a standard FE to the point
 701 that many CMOS MAPS detectors used a similar FE and are called "ALPIDE-like". Considering
 702 that both TJ-Monopix1 and ARCADIA-MD1 have an ALPIDE-like FE, I am going to explain the
 broad principles of the early FE stage. The general idea is of the amplification to transfer the



Parameter	Meaning	
IBIAS	mainly controls the rise time	yes? check
IDB	sets the discriminator threshold	yes
ITHR	sets the velocity of the return to the baseline	yes
ICASN	sets the baseline of the signal	yes
VRESET	sets the gain of the preamplifier	yes
IRESET	sets the gain of the preamplifier	no

Table 4.3: FE parameters which must be setted through the DAQ. "Function" means that higher parameter implies higher value

704 charge from a bigger capacity[14], C_{source} , to a smaller one, C_{out} : the input transistor M1 with
 705 current source IBIAS acts as a source follower and this forces the source of M1 to be equal to the
 706 gate input $\Delta V_{PIX_IN} = Q_{IN}/C_{IN}$.

$$Q_{source} = C_{source} \Delta V_{PIX_IN} \quad (4.1)$$

707 The current in M2 and the charge accumulates on C_{out} is fixed by the one on C_{source} :

$$\Delta V_{OUT_A} = \frac{Q_{source}}{C_{OUT_A}} = \frac{C_{source} \Delta V_{PIX_IN}}{C_{OUT_A}} = \frac{C_{source}}{C_{OUT_A}} \frac{Q_{IN}}{C_{IN}} \quad (4.2)$$

708 A second branch (M4, M5) is used to generate a low frequency feedback, where VCASN and ITHR
 709 set the baseline value of the signal on C_{OUT_A} and the velocity to goes down to the baseline.

IL RUOLO DI CURVFEED NON L'HO CAPITO.

711 Finally IDB defines the charge threshold with which the signal OUT_A must be compared: de-
 712 pending on if the signal is higher than the threshold or not, the OUT_D is high or low respectively.

713 The actual circuit implemented in TJ-Monopix1 is shown in figure 4.5b: the principal difference
 714 lays in the addition of disableing pixels' readout. This possibility is uttermost important in order to
 715 reduce the hit rate and to avoid saturating the bandwidth due to the noisy pixels, which typically
 716 are those with manufacturing defects. In the circuit transistors M8, M9 and M10 have the function
 717 of disabling registers with coordinates MASKH, MASKV and MASKD (respectively vertical, ori-
 718 ental and diagonal) from readout: if all three transistors-signals are low, the pixel's discriminator
 719 is disabled. Compared with a configurable masking register which would allow disableing pixels
 720 individually, to use a triple redundancy reduces the sensistivity to SEU but also gives amount of
 721 intentionally masked ("ghost") pixels. This approach is suitable only for extremely small number
 722 N of pixel has to be masked: if two coordinate projection scheme had been implemented, the
 723 number of ghost pixels would have scale with N^2 , if instead three coordinates are used, the N's
 exponential is lower than 2 (fig. 4.6)

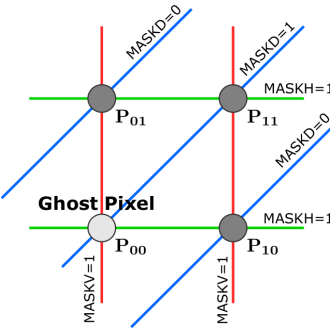


Figure 4.6

724

4.3 Readout logic

726 TJ-Monopix1 has a triggerless, fast and with ToT capability R/O which is based on a column-drain
 727 architecture. On the pixel are located two Random Access Memory (RAM) cells to store the 6-bit

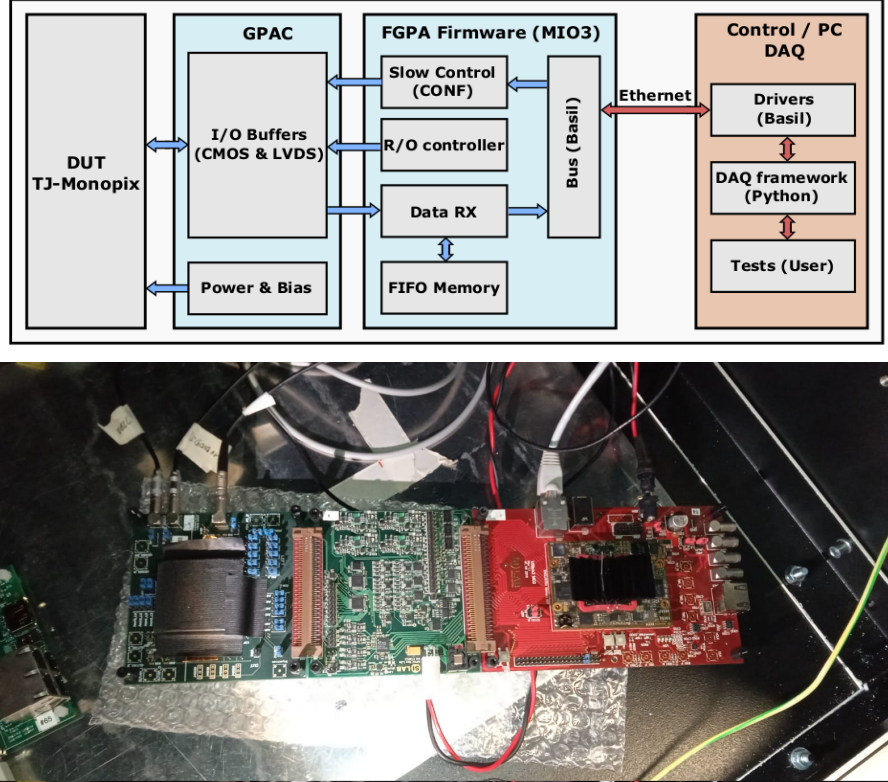
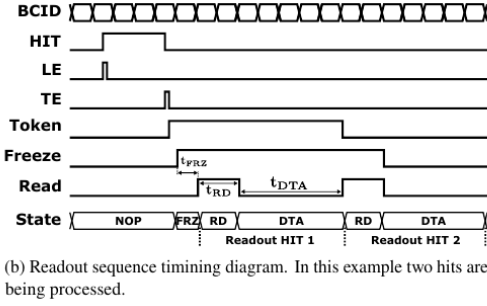


Figure 4.7: Main caption

728 LE and 6-bit TE of the pulse, and a Read-Only Memory (ROM) containing the 9-bit pixel address.
 729 Excluded these memories, TJ-Monopix1 hasn't any other buffer: if a hit arrives while the pixel is
 730 already storing a previous one, the new data get lost. After being read, the data packet is sent to
 731 the EoC periphery of the matrix, where a serializer transfers it off-chip to an FPGA (4.7). There
 732 a FIFO is used to temporarily stored the data, which is transmitted to a computer through an
 733 ethernet cable in a later time.

734 The access to the pixels' memory and the transmission of the data to the EoC, following
 735 a priority chain, is managed by control signals and is based on a Finite State Machine (FSM)
 736 composed by four state: no-operation (NOP), freeze (FRZ), read (RD) and data transfer (DTA).
 737 The readout sequence (??) starts with the TE of a pulse: the pixel immediately tries to grab the
 738 column-bus turning up a hit flag signal called *token*. The token is used to control the priority chain
 739 and propagates across the column indicating what pixel that must be read. To start the readout
 740 and avoid that the arrival of new hits disrupt the priority logic, a *freeze* signal is activated, and
 741 then a *read* signal controls the readout and the access to memory. During the freeze, the state of
 742 the token for all pixels on the matrix remains settled: this does not forbid new hits on other pixels
 743 from being recorded, but forbids pixels hit from turning on the token until the freeze is ended. The
 744 freeze stays on until the token covers the whole priority chain and gets the EoC: during that time
 745 new token cannot be turned on, and all hits arrived during a freeze will turn on their token at the
 746 end of the previous freeze. Since the start of the token is used to assign a timestamp to the hit,
 747 the token time has a direct impact on the time resolution measurement; this could be a problem
 748 coping with high hits rate.

749 The analog FE circuit and the pixel control logic are connected by an edge detector which is
 750 used to determine the LE and the TE of the hit pulse(fig. 4.9): when the TE is stored in the first
 751 latch the edge detector is disabled and, if the **FREEZE** signal is not set yet, the readout starts. At
 752 this point the HIT flag is set in a second latch and a token signal is produced and depending on
 753 the value of **Token in** the pixel can be read or must wait until the **Token in** is off. In figure an OR
 754 is used to manage the token propagation, but since a native OR logic port cannot be implemented
 755 with CMOS logic, a sum of a NOR and of an inverter is actually used; this construct significantly
 756 increases the propagation delay (the timing dispersion along a column of 0.1-0.2 ns) of the token



(b) Readout sequence timing diagram. In this example two hits are being processed.

Figure 4.8: Readout timing diagram: in this example two hits are being processed

and to speed up the circuit optimized solution are often implemented. When the pixel become the next to be read in the queue, and at the rising edge of the **READ** signal, the state of the pixel is stored in a D-latch and the pixel is allowed to use the data bus; the TE and the HIT flag latches are reset and a **READINT** signal that enable access of the RAM and ROM cells is produced.

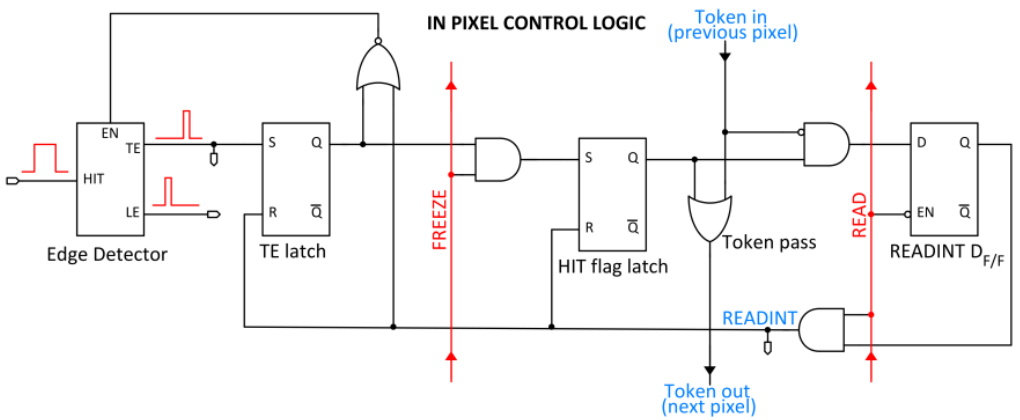


Figure 4.9

The final data must provide all the hits' information: the pixel address, the ToT and the timestamp. All those parts are assigned and appended at different time during the R/O chain:

- **Pixel address:** while the double column address (6-bit) is appended by the EoC circuit, the row address (8-bits for each flavor) and the physical column in the doublet (1-bit) are assigned by the in-pixel logic
- **ToT:** is obtained offline from the difference of 6-bits TE and 6-bits LE, stored by the edge detector in-pixel; since a 40 MHz BCID is distributed across the matrix, the ToT value is range 0-64 clock cycle which corresponds to 0-1.6 μ s
- **Timestamp:** The timestamp of the hit correspond to the time when the pixel set up the token; it is assigned by the FPGA, that uses the LE, TE and a 640 MHz clock to derive it. For all those hits which arrived while the matrix is frozen, the timestamp is no more correlated with the time of arrival of the particle

When the bits are joined up together the complete hit data packet is 27-bit.

775 Chapter 5

776 Arcadia-MD1

777 [15] [16]

778 Breve introduzione analoga a Monopix1 in cui descrivo brevemente la "timeline" da SEED
779 Matisse a Md1 e Md2

780 5.1 The sensor

781 ARCADIA-MD1 is an LFoundry chip which implements the technology 110 nm CMOSS node
782 with six metal layer ???. The standard p-type substrate was replaced with an n-type floating zone
783 material, that is a tecnique to produce purified silicon crystal. (pag 299 K.W.).

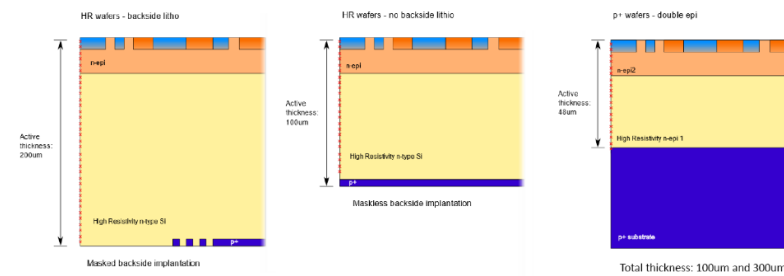


Figure 5.1

784
785 Wafer thinning and backside litography were necessary to introduce a junction at the bottom
786 surface, used to bias the substrate to full depletion while maintaining a low voltage at the front side.
787 C'è un deep pwell per - priority chainseparare l'elettronica dal sensore; per controllare il punchthought
788 è stato aggiunto un n doped epitaxial layer having a resistivity lower than the substrate.

789 RILEGGI SUL KOLANOSKY COS'È IL PUNCHTHROUGHT, FLOAT ZONE MATERIAL,
790 COME VENGONO FATTI I MAPS COME FAI LE GIUNZIONI

791 It is part of the cathegory of DMAPS Small electrode to enhance the signal to noise ratio.
792 It is operated in full depletion with fast charge collection by drift.

793 Prima SEED si occupa di studiare le prestazioni: oncept study with small-scale test struc-
794 ture (SEED), dopo arcadia: technology demonstration with large area sensors Small scale demo
795 SEED(sensor with embedded electronic developement) Quanto spazio dato all'elettronica sopra il
796 pwell e quanto al diodo. ..

797 5.2 Readout logic and data structure

798 5.2.1 Matrix division and data-packets

799 The matrix is divided into an internal physical and logical hierarchy: The 512 columns are divided
800 in 16 section: each section has different voltage-bias + serializzatori. Each section is devided in

801 cores () in modo che in ogni doppia colonna ci siano 1Pacchetto dei dati 6 cores. ricordati dei serializzatori: sono 16 ma possono essere ridotti ad uno in modalità spazio

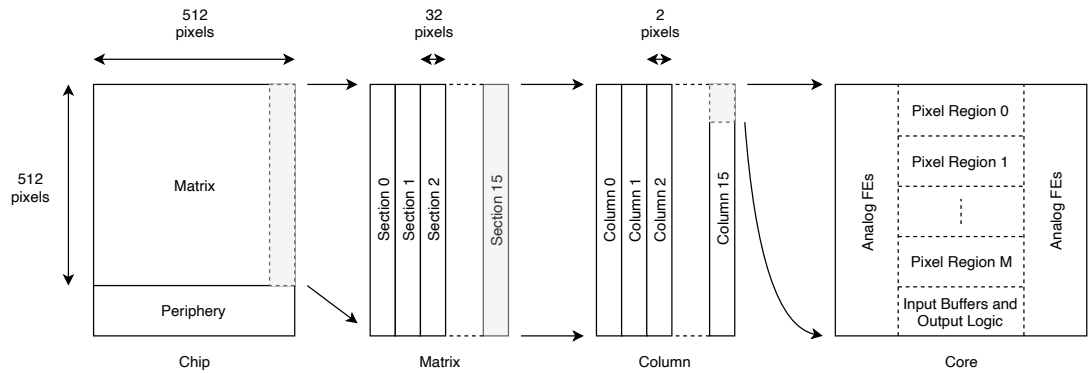


Figure 5.2

802

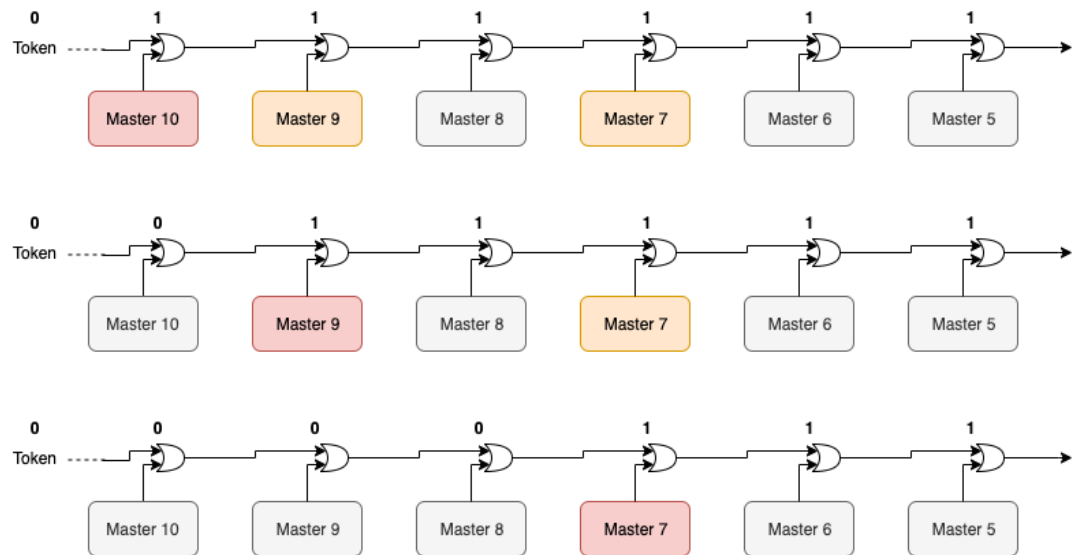


Figure 5.3

803 Questa divisione si rispecchia in come sono fatti i dati: scrivi da quanti bit un dato è fatto e le
804 varie coordinate che ci si trovano dentro; devi dire che c'è un pixel hot e spieghi dopo a cosa serve,
805 e devi accennare al timestamp

806 "A core is simply the smallest stepped and repeated instance of digital circuitry. A relatively
807 large core allows one to take full advantage of digital synthesis tools to implement complex func-
808 tionality in the pixel matrix, sharing resources among many pixels as needed.". pagina 28 della
809 review.

810

811 TABELLA: con la gerarchia del chip Matrix (512x512 pixels) Section (512x32 pixels) Column
812 (512x2) Core (32x2) Region (4x2)

813 Nel chip trovi diverse padframe: cosa c'è nelle padframe e End of section.

814 "DC-balance avoids low frequencies by guaranteeing at least one transition every n bits; for
815 example 8b10b encoding n =5"

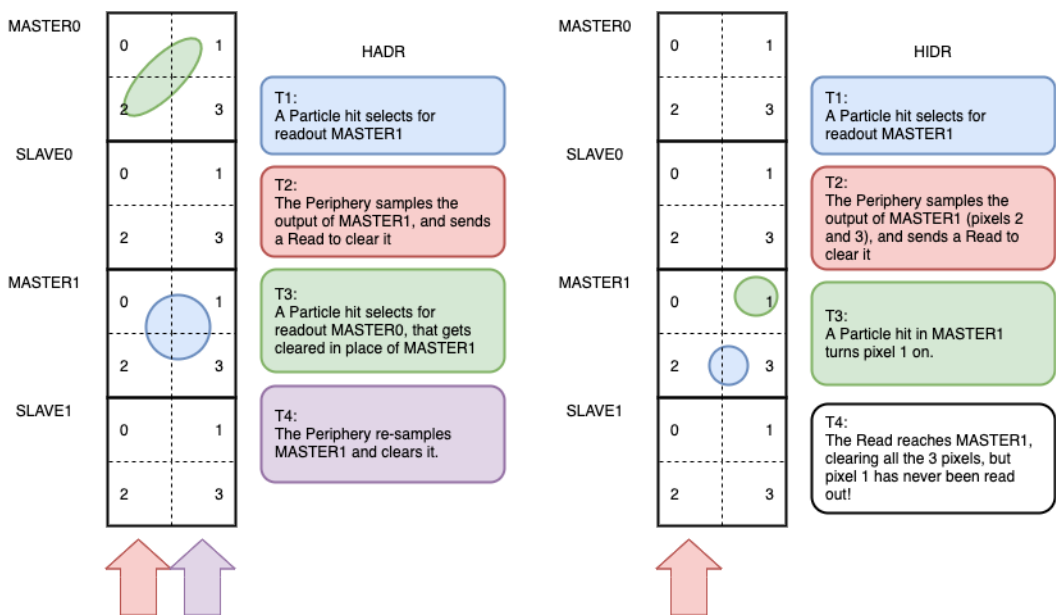


Figure 5.4

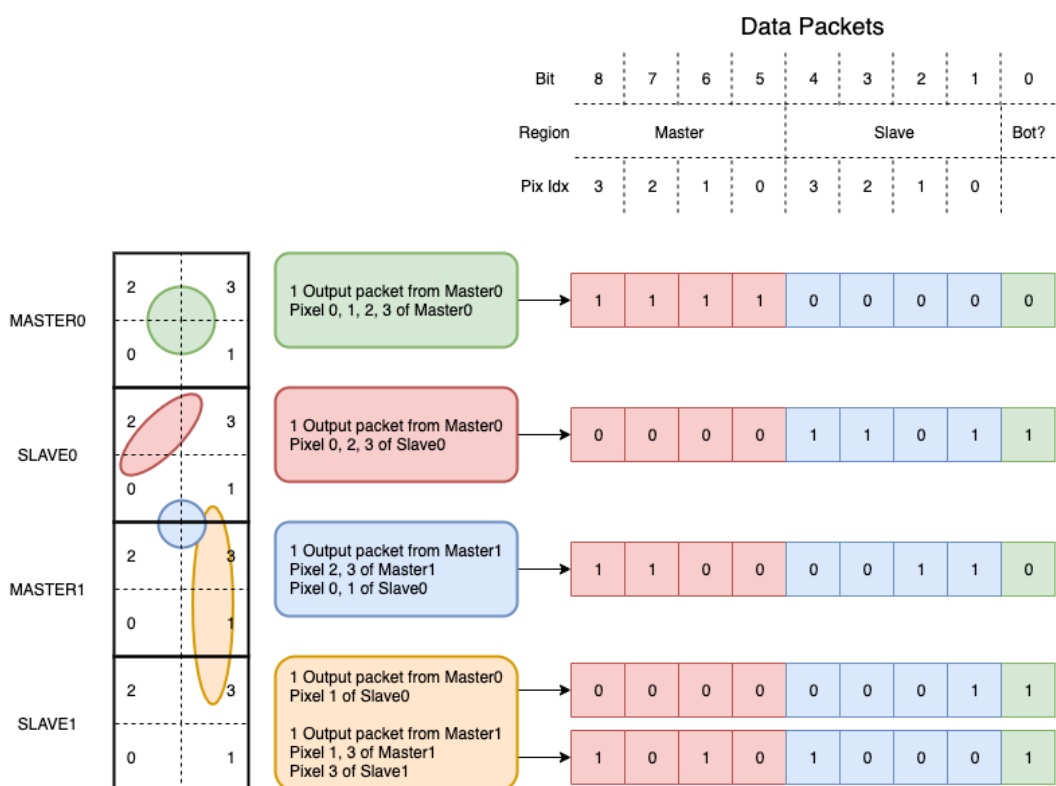


Figure 5.5

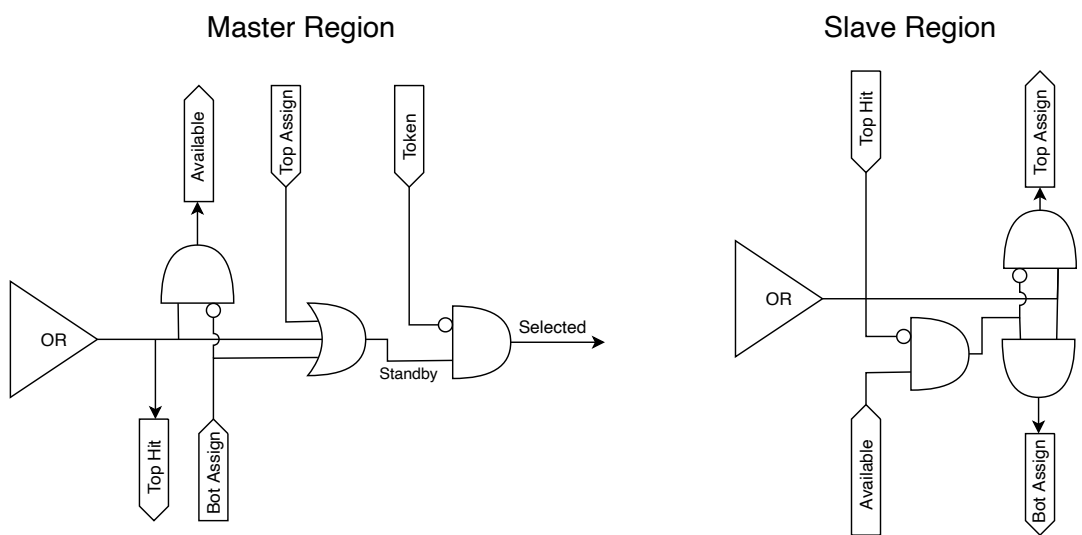


Figure 5.6

816 **Chapter 6**

817 **Threshold and noise
characterization**

819 **6.1 TJ-Monopix1 characterization**

820 **6.1.1 Threshold and noise: figure of merit for pixel detectors**

821 The threshold has to be high enough to cut the noise, but also low enough to mantain a high
822 signal efficiency, and For low enough threshold and/or enough pixels firing at the same time, this
823 positive feedback can set off a chain reaction causing all pixels to fire. For a given instantaneous
824 hit occupancy (fraction of pixels firing atthe same time due to an external stimulus), there will be
825 a minimum stable threshold. For this reason the signal to threshold ratio, rather than the signal
826 to noise ratio, can be considered as the figure of merit for pixel detectors.

827 la soglia è collegato al rumore, nel senso che: supponiamo di volere un occupancy di 10-4 allora
828 sceglierò la soglia in base a questo. (plot su quaderno) Da questo conto trovo la minima soglia
829 mettibile

830 In realtà quello che faccio è mettere una soglia un po' più grande perchè il rate di rumore dipende
831 da molti fattori quali la temperatura, l annealing ecc, e non voglio che cambiando leggermente uno
832 di questi parametri vedo alzarsi molto il rate di rumore. In realtà non è solo il rumore sensibile a
833 diversi fattori, ma anche la soglia: ad esempio la cosa classica è la variabilità della soglia da pixel
834 a pixel.

835 In questo modo rumore e soglia diventano parenti.

836 The front end noise does set a lower bound to the threshold, but does not determine how far
837 above this lower bound is the minimum stable threshold. Assuming a noise occupancy of 10meno4
838 is acceptable, this corresponds to the Gaussian 1-sided tail fraction for 3.7sigma . Inverting the
839 question, for a 500 e minimum threshold, the noise must be less than 500/3.7=135 e equivalent
840 input charge. But this is just an upper bound. How far below this bound the noise needs to be
841 depends on how the threshold varies with time and how frompixel to pixel.

843 Questo implica tra le altre cose che voglio poter assegnare delle soglie diverse a diversi pixel.
844 Non fare trimming sulla soglia è uno dei problemi che si sono sempre incontrati: a casusa dei
845 mismatch dei transistor le soglie efficaci pixel per pixel cambiano tanto.

846 ASSEGNAZIONE DELLE SOGLIE IN TJ MONOPIX E ARAVDIA. Drawback è dare spazio
847 per registri e quantaltro. Ad esempio per Monopix1 la soglia è locale, poi 3 bit vengono allocati per
848 trimming sul singolo pixel. Arcadia invece Questo lascia però ancora aperto il problema tempo-
849 riale delle variazioni del rumore: problema per cui diventano necessarie le misure dei sensori dopo
850 l'irraggiamento.

851 La larghezza della s curve è il noise se assumi che il noise è gaussiano
852 Il trimming della soglia avviene con dei DAC: la dispersione della soglia dopo al tuning e dovuta
853 al dac è:

$$\sigma_{THR,tuned} = \frac{\sigma_{THR}}{2^{nbit}} \quad (6.1)$$

855 dove il numero di bit cambia varia tra 3-7 tipicamente. Monopix è 7 Arcadia 6

	DAC units	electrons
Threshold	24.529 ± 0.049 u: 24.433 ± 0.049 d: 24.623 ± 0.051	
Threshold dispersion	1.848 ± 0.033 u: 1.867 ± 0.034 d: 1.825 ± 0.035	
Noise	0.8222 ± 0.0043 u: 0.8225 ± 0.0045 d: 0.8221 ± 0.0043	
Noise dispersion	0.0975 ± 0.0030 u: 0.0968 ± 0.0031 d: 0.0970 ± 0.0030	

Table 6.1: Flavor PMOS

856
857 Each ROIC is different in this respect, but in general the minimum stable threshold was around
858 2500 electrons (e) in 1st generation ROICs, whereas it will be around 500 e for the 3rd generation.
859 This reduction has been deliberate: required by decreasing input signal values. Large pixels (2 104
860 um²), thick sensors (maggiori di 200 um), and moderate sensor radiation damage for 1st generation
861 detectors translated into expected signals of order 10 ke, while small pixels (0.25 104 um²), thinner
862 sensors (100 um), and heavier sensor radiation damage will lead to signals as low as 2 ke at the
863 HL-LHC
864 The ENC can be directly calculated by the Cumulative Distribution Function (CDF) (scurve)
865 obtained from the discriminator "hit" pulse response to multiple charge injections
866 Radiation damages oxide layer causes shift of MOSFET threshold voltage

$$f(x, \mu, \sigma) = \frac{1}{2} \left(1 + \operatorname{erf} \left(\frac{x - \mu}{\sigma \sqrt{2}} \right) \right) \quad (6.2)$$

$$\operatorname{erf}(z) = \frac{2}{\sqrt{\pi}} e^{-z^2} dx \quad (6.3)$$

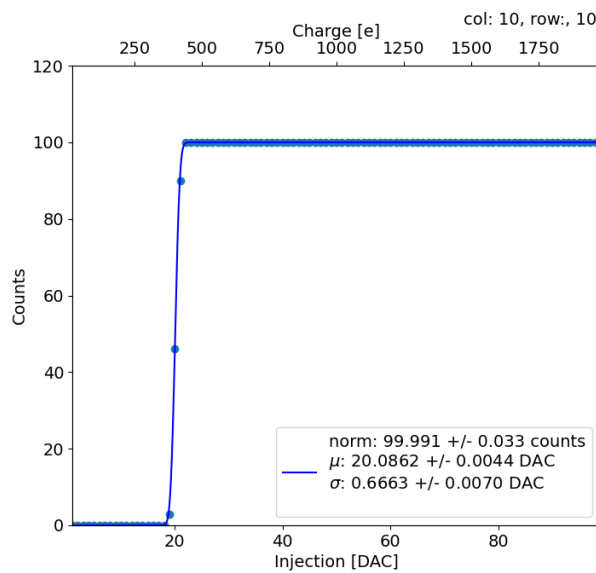
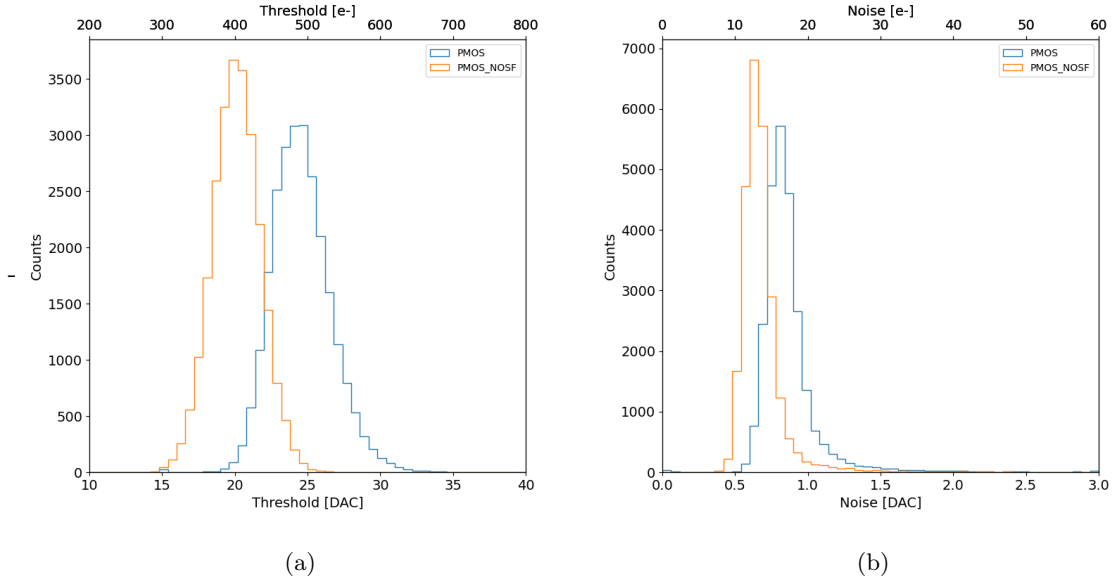
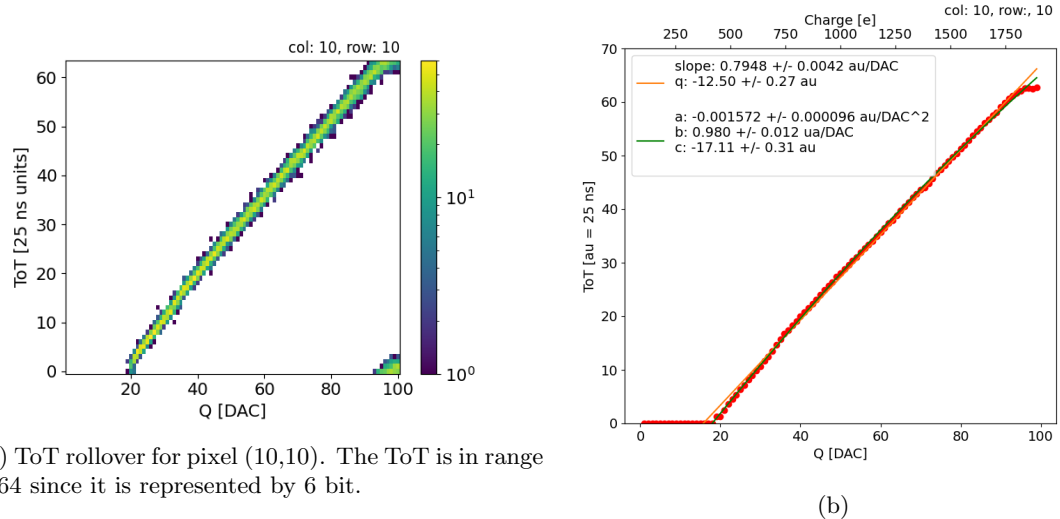


Figure 6.1: S curve for pixel (10, 10) of the PMOS flavor



868 6.1.2 Calibration of the ToT



869 Absolute calibration

$$f(x, m, q, N, \mu, \sigma) = m x + q + \frac{N}{\sigma \sqrt{2\pi}} e^{-\frac{1}{2} \left(\frac{(x-\mu)}{\sigma}\right)^2} \quad (6.4)$$

870 Mappa dei parametri del fit sulla matrice (media e sigma)

871 6.2 Fe vs bias

- 872 • rate vs bias
- 873 • posizione del picco del ferro vs bias
- 874 • eventi sotto il picco vs eventi nella coda

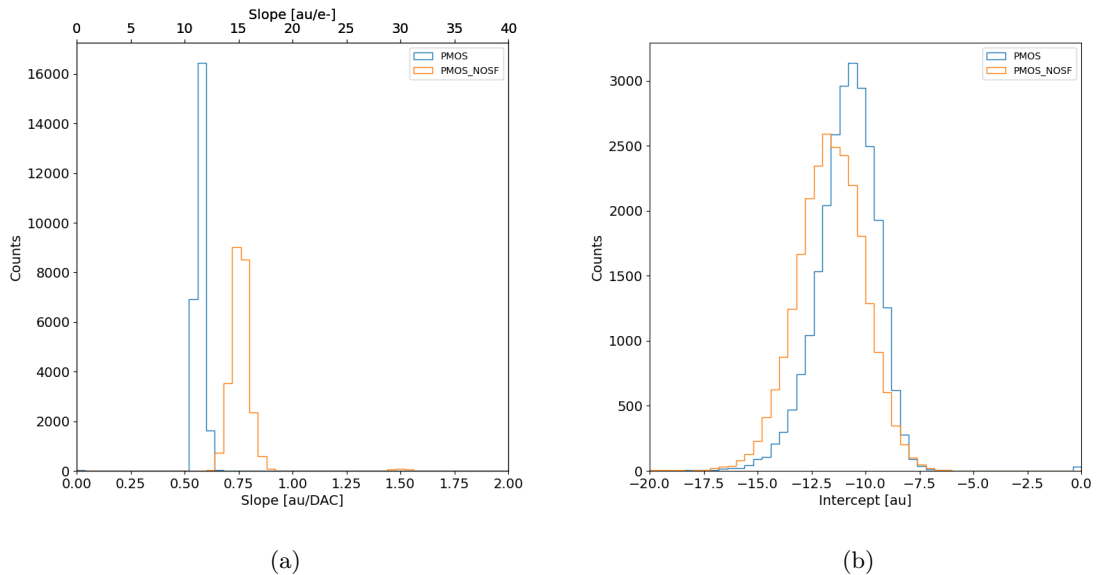


Table 6.2

	PMOS	HV
Slope [au/DAC]	0.57145 ± 0.00025	
Slope dispersion [au/DAC]	0.01685 ± 0.00016	
Intercept [au]	-10.824 ± 0.019	
Intercept dispersion [au]	1.225 ± 0.013	

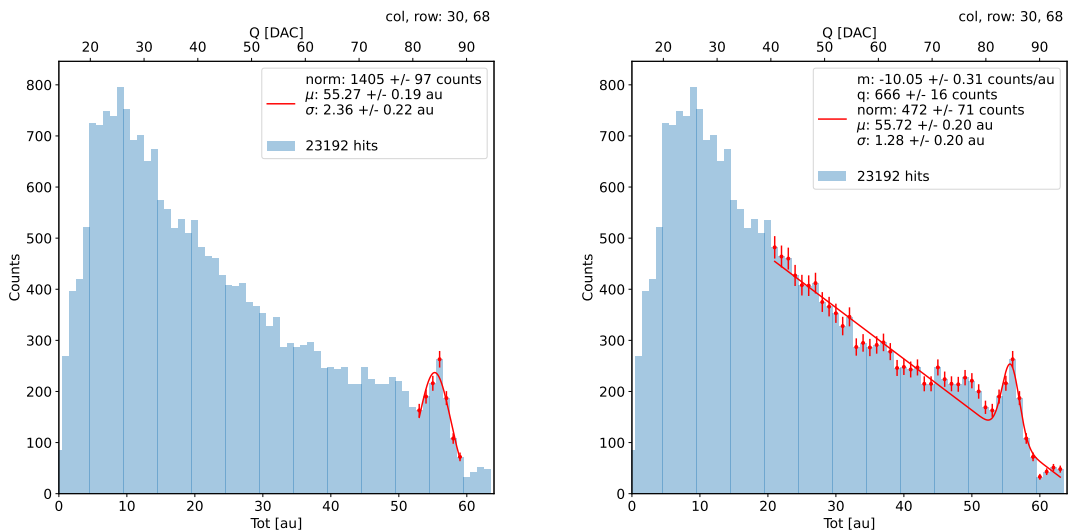


Figure 6.5: due pixel per far vedere la differenza tra i fit

875 6.3 Measurements with radioactive sources

876 CI metterei i plot con ferro, stronzio e cosmici ToT con doppia scala (calibrata in elettroni e non
877 in ToT) hit per cluster dimensione cluster hit map di un paio di tracce?

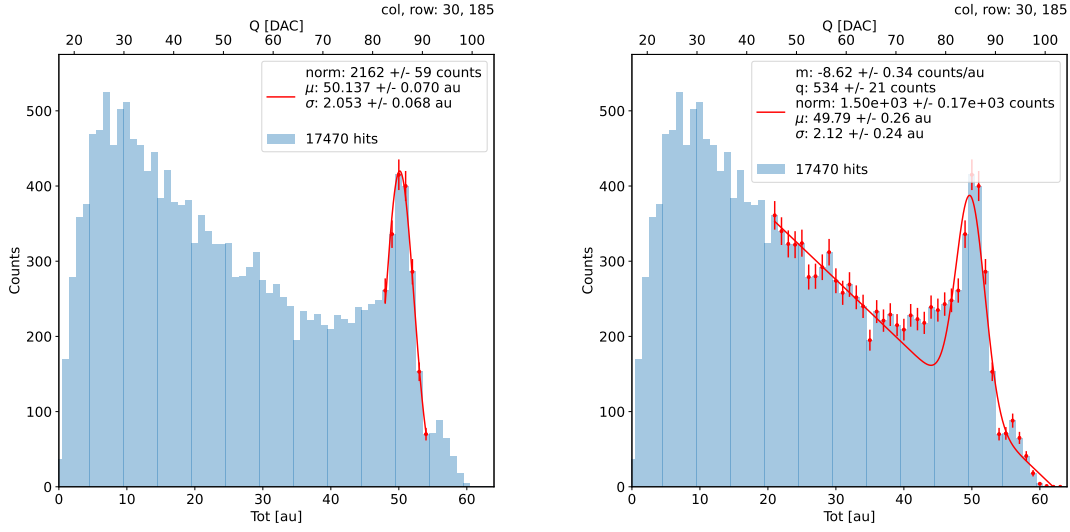


Figure 6.6: due pixel per far vedere la differenza tra i fit

6.3.1 Dead time measurements

The hit loss is due to analog and digital pile up: the first one occurs when a new hit arrives during the pre-amplifier response, the second instead, which is the more relevant contribution with high rate, while the information of the previous hit has not yet been transferred to the periphery. As only one hit at a time can be stored on the pixel's RAM, until the data have completed the path to get out, the pixel is paralyzed and the dead time τ almost corresponds with the time needed to transmit the data-packets off-chip. Since the exportation of data from pixel to the EoC occurs via a 21-bits data bus, only one clock cycle is need to transfer the data to the end of column and the dead time bottleneck is given by the bandwidth of the serializer at the EoC. In our setup the serializer operates at 40 MHz, thus to transmit a data packet (27-bit considering the addition at the EoC) at least 675 ns are needed. For what we have said so far, the R/O is completely sequential and therefore is expected a linear dependence of the reading time on the number of pixels to read:

$$\tau = 25 \text{ ns} \times (\alpha N + \beta) \quad (6.5)$$

where α and β are parameters dependent on the readout chain setting.

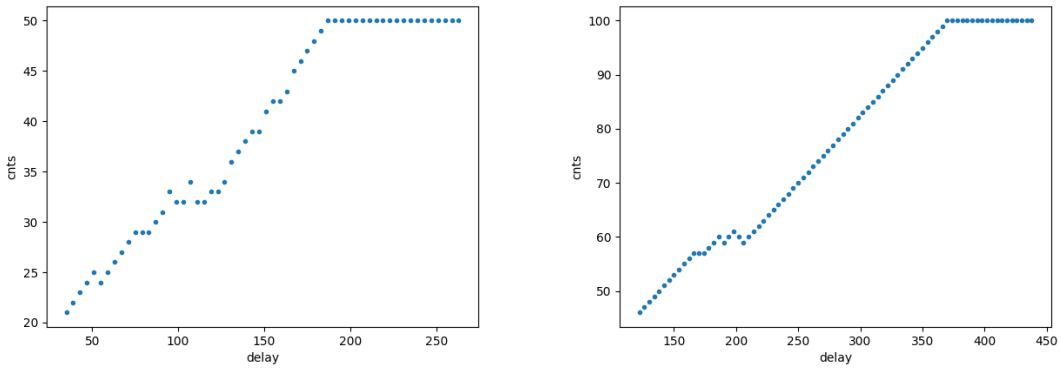
To measure and test the linearity of the reading time with the number of pixels firing, I have used the injection mode available on the chip. Indeed, the injection mode allows fixing not only the amplitude of the pulse, which corresponds to the charge in DAC units, but also the period and the width. I have injected a fix number of pulses (100) and looked for the rate when the efficiency decreases. Moreover to test that there is no dependece of the digital readout time from the charge of the pulse, I have try to change the amplitude of the pulse injected, but the parameters found were consistent with the default configuration ones.

Al posto degli esempi con 5 e 10 pixels metterei un esempio dell'efficienza vs il periodo quando leggo un singolo pixel. Una cosa che volevo fare era anche provare a fittare la slope con cui l'efficienza scende: se la slope è uguale per tutti il readout diventa completamente predittivo.

While the single pixel reading time and the dead time do not depend on the position on the pixel matrix and are equal to 106 (46+60) clock counts within 1 clock count, on the other hand the τ depends on the pixel position on the matrix when more than one pixel are firing. In particular the priority chain goes from row 224 to row 0, and from col 0 to 112, that means the last pixels to be read is the one on le bottom right corner of the matrix.

In figure 6.9 is reported the reading time versus the number of pixels injected; the R/O parameters that control the reading time and their default values are reported on table ??.

The factor α , referring to eq. 6.5 is proportional to the difference (STOP_FREEZE - START_READ), while the offset β lies between 5 and 15 clock counts. Since through the injection a random hit rate on the matrix can't be simulated, as the coordinates of the pixels to inject must be specified, for



(a) efficiency vs DELAY 5 pixels

(b) efficiency vs DELAY per 10pixels

Parameter	Value [DAC]	Value [μ s]
START_FREEZE	64	1.6
STOP_FREEZE	100	2.5
START_READ	66	1.65
STOP_READ	68	1.7

Table 6.3: Default configuration of the R/O parameters

convenience I used the pixels on the same column/row. No difference in the α and β coefficients has been observed between the two case.

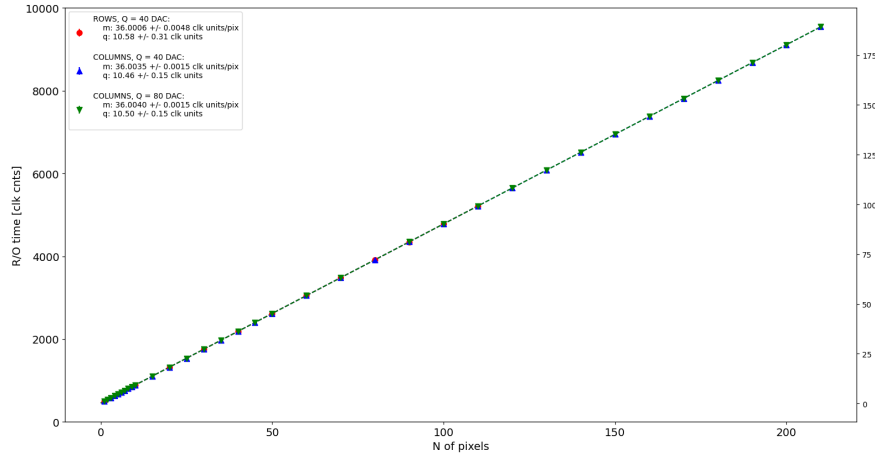


Figure 6.8

Ci sarebbe da spiegare perchè i parametri che usiamo noi come default non sono quelli che minimizzano il tempo di lettura. La spiegazione è che "Abbiamo copiato i valori dal repository di quelli di Bonn". Un'altra domanda potrebbe essere: come mai non ho esplorato una zona più vasta per i parametri del R/O. Cambiando molto i parametri del R/O la lettura non funzionava per niente: ad esempio CONF_STOP_FREEZE non può essere impostato nè sopra 105 nè sotto 95

6.4 ARCADIA-MD1 characterization

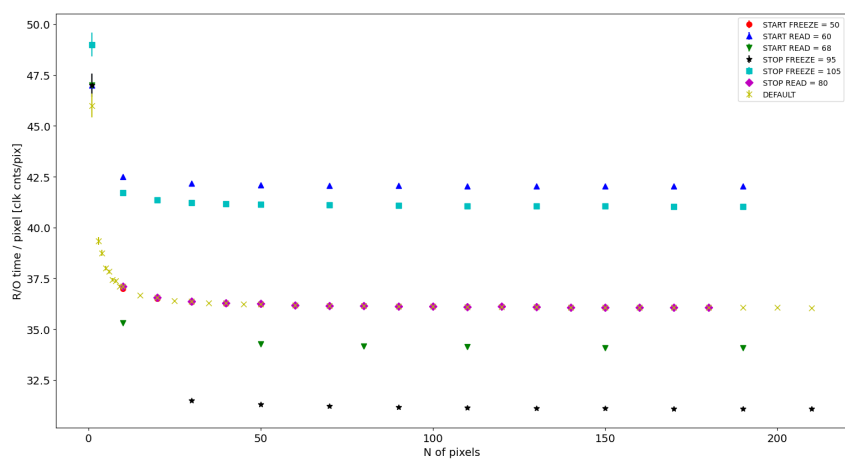


Figure 6.9

919 **Chapter 7**

920 **Test beam measurements**

921 **7.1 Testbeam motivation**

922 Possibilità di integrare carica sul pixel: due elettroni consecutivi su un pixel ogni quanto arrivano?

923 Vogliamo sfruttare l'analog pile up, per fare questo dobbiamo fare attenzione a non finire nel
924 digital pile up Devi avere che il tot dell'elettrone (cioè MIP) è maggiore del deltat medio; in questo
925 caso potresti riuscire ad integrare carica. Non è possibile rivelare singoli elettroni in quanto l'hit
926 rate è troppo alto per le dosi messe a disposizioni con il fascio. Una formula di conversione è:

$$R[Hz/cm^2] = \frac{DPP[Gy]}{1.6 \cdot 10^{10} S[g/cm^2]} \quad (7.1)$$

927 where S is the stopping power in water, $2.17 g/cm^2$ The medium is ordinarily water, since dosimetric
928 protocols are based on measurements in water as reference

929 La struttura del fascio e le varie quantità che si usano per descriverlo sono riportate in figure
930 7.1. Ricordo i valori tipici che stanno in tabella in table ??.

931 **7.2 Apparatus description**

932 **7.3 Measurements**

933 Numero di hit in funzione del DDP. Spettri con e senza collimatori.

Table 1. Terminology used throughout the text.

Term	Symbol	Description
intra-pulse dose-rate	—	The duration of a single pulse. ^a
	\bar{D}	Mean dose-rate for a multi-pulse delivery.
pulse repetition frequency	\dot{D}_p	Dose-rate in a single pulse. ^a
	DPP	Dose in a single pulse. ^a
	PRF	Number of pulses delivered per unit time. ^a
	t_i	Total irradiation time from the beginning of the first delivered pulse to the end of the last delivered pulse.
ultrahigh dose-rate	—	Radiation delivered with mean dose-rate of $> \sim 40 \text{ Gy s}^{-1}$.
	—	Ultrahigh dose-rate RT that presents decreased damage to normal tissues compared to RT delivered with conventional dose-rate of $\sim 0.04 \text{ Gy s}^{-1}$.

^aPulses are considered to be macro-pulses unless otherwise stated (see also figure 1).

^bIn literature sometimes referred to as the instantaneous dose-rate.

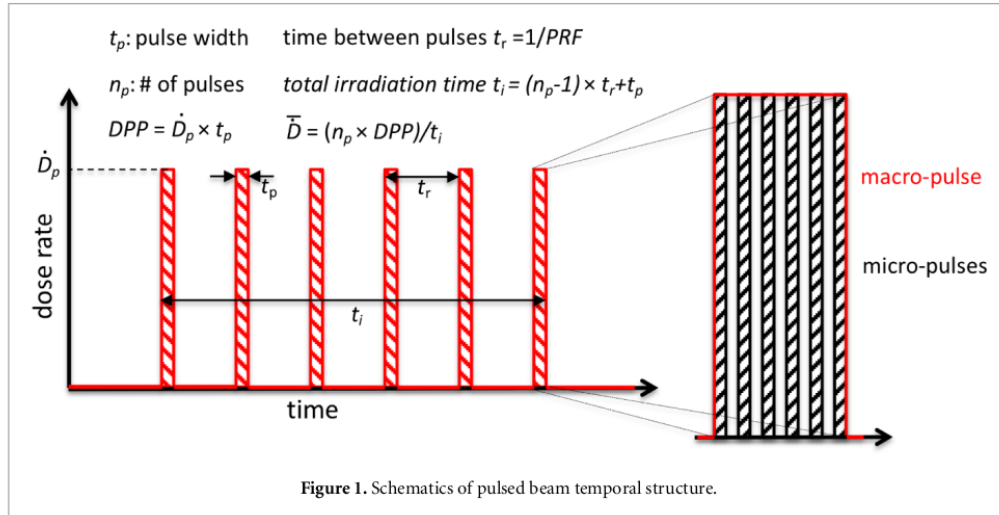


Figure 7.1

934 Appendix A

935 Pixels detector: a brief overview

936 A.1 Radiation damages

937 Radiation hardness is a fundamental requirement for pixels detector especially in HEP since they
 938 are almost always installed near the interaction point where there is a high energy level of radiation.
 939 At LHC the ϕ_{eq} per year in the innermost pixel detector is $10^{14} n_{eq}/cm^2$; this number reduces by
 940 an order passing to the outer tracker layer [2] pag 341 Wermes. Here the high fluence of particles
 941 can cause a damage both in the substrate of the detector and in the superficial electronics.

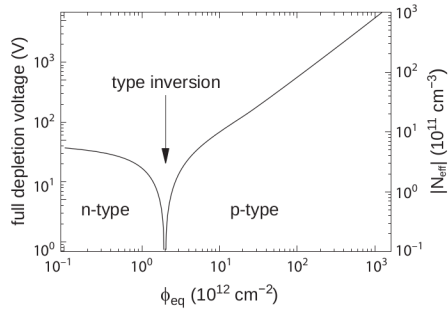
942 The first one has a principal non ionizing nature, due to a non ionizing energy loss (NIEL), but
 943 it is related with the dislocation of the lattice caused by the collision with nuclei; by this fact the
 944 NIEL hypothesis states that the substrate damage is normalized to the damage caused by 1 MeV
 945 neutrons. Differently, surface damages are principally due to ionizing energy loss.

946 **DUE PAROLE IN PIÙ SUL SURFACE DAMAGE** A charge accumulation in oxide (S_iO_2) can
 947 cause the generation of parasitic current with an obvious increase of the 1/f noise. Surface damages
 948 are mostly less relevant than the previous one, since with the development of microelectronics and
 949 with the miniaturization of components (in electronic industry 6-7 nm transistors are already used,
 950 while for MAPS the dimensions of components is around 180 nm) the quantity of oxide in circuit
 951 is reduced.

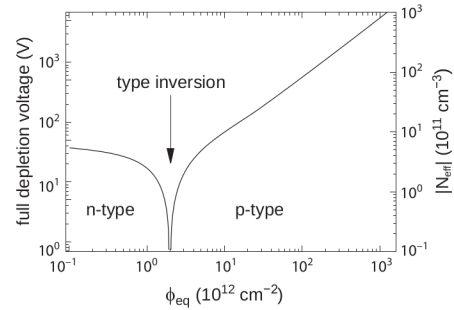
952 Let's spend instead two more other words on the more-relevant substrate damages: the general
 953 result of high radiation level is the creation of new energy levels within the silicon band gap and
 954 depending on their energy-location their effect can be different, as described in the Shockely-Read-
 955 Hall (SRH) statistical model. The three main consequence of radiation damages are the changing
 956 of the effect doping concentration, the leakage current and the increasing of trapping probability.

957 **Changing of the effective doping concentration:** is associated with the creation/removal
 958 of donors and acceptors center which trap respectively electrons/holes from the conduction band
 959 and cause a change in effective space charge density. Even an inversion (p-type becomes n-type¹)
 960 can happen: indeed it is quite common at not too high fluences ($\phi_{eq} 10^{12-13} n_{eq} cm^{-2}$). A changing
 961 in the doping concentration requires an adjustment of the biasing of the sensor during its lifetime
 962 (eq.2.1) and sometimes can be difficult keeping to fully deplete the bulk.

¹L'INVERSIONE OPPOSTA NON CE L'HA PERCHÈ?



(a) 1a



(b) 1b

963 **Leakage current:** is associated with the generation-recombination centers. It has a strong
964 dependence with the temperature ($I_{leak} \propto T^2$), whose solution is therefore to operate at lower
965 temperature.

966 **Increase of trapping probability:** since the trapping probability is constant in the depleted
967 region, the collected charge decreases exponentially with the drift path. The exponential coefficient,
968 that is the mean trapping path, decreases after irradiation and typical values are 125-250 μm and
969 must be compared with the thickness of the depleted region which () corresponds to the mean drift
970 path.

971 Different choices for substrate resistivity, for junctions type and for detector design are typically
972 made to fight radiation issues. Some material with high oxygen concentration (as crystal produced
973 using Czochralki (Cz) or float-zone (Fz) process (**CONTROLLA LA DIFFERENZA TRA I DUE**))
974 for example, show a compensation effect for radiation damage; another example is the usage of
975 n+ -in-p/n sensors (even if p+ -in-n sensors are easier and cheaper to obtain) to get advantage
976 of inversion/to have not the inversion (since they are already p-type). After inversion the n+p
977 boundary, coming from n+ in-n, but to keep using the sensor the depletion zone still must be
978 placed near the diode.

979 Single Event Upset, in sostanza è quando un bit ti cambia valore (da 0 a 1 o viceversa) perché
980 una particella deposita carica nell'elettronica che fa da memoria registro/RAM/.... Questo tipo
981 di elettronica ha bisogno di un sacco di carica prima che il bit si "flippi" (cambi valore), infatti
982 tipicamente per avere un SEU non basta una MIP che attraversa esattamente quel pezzo di chip
983 in cui è implementata la memoria, ma un adrone che faccia interazione nucleare producendo più
984 carica di quanto farebbe una MIP. Questo metodo pur essendo più comodo richiede less amount of
985 area ha però come drawback che il registro può essere soggetto a SEU problema non trascurabile
986 in acceleratori come HL-LHC adronici

987 Bibliography

- 988 [1] W. Snoeys et al. “A process modification for CMOS monolithic active pixel sensors for
989 enhanced depletion, timing performance and radiation tolerance”. In: (2017). DOI: <https://doi.org/10.1016/j.nima.2017.07.046>.
- 990 [2] H. Kolanoski and N. Wermes. *Particle Detectors: Fundamentals and Applications*. OXFORD
991 University Press, 2020. ISBN: 9780198520115.
- 992 [3] E. Mandelli. “Digital Column Readout Architecture for 10.1109/NSSMIC.2009.5402399 the
993 ATLAS Pixel 0.25 um Front End IC”. In: (2002).
- 994 [4] M. Garcia-Sciveres and N. Wermes. “A review of advances in pixel detectors for experiments
995 with high rate and radiation”. In: (2018). DOI: <https://doi.org/10.1088/1361-6633/aab064>.
- 996 [5] C. Marinas. “The Belle-II DEPFET pixel detector: A step forward in vertexing in the su-
997 perKEKB flavour factory”. In: (2011). DOI: [doi:10.1016/j.nima.2010.12.116](https://doi.org/10.1016/j.nima.2010.12.116).
- 1000 [6] J. Baudot. “First Test Results Of MIMOSA-26, A Fast CMOS Sensor With Integrated Zero
1001 Suppression And Digitized Output”. In: (2010). DOI: [doi:10.1109/NSSMIC.2009.5402399](https://doi.org/10.1109/NSSMIC.2009.5402399).
- 1002 [7] A. Dorokhov. “High resistivity CMOS pixel sensors and their application to the STAR PXL
1003 detector”. In: (2011). DOI: [doi:10.1016/j.nima.2010.12.112](https://doi.org/10.1016/j.nima.2010.12.112).
- 1004 [8] Giacomo Contin. “The STAR MAPS-based PiXeL detector”. In: (2018). DOI: <https://doi.org/10.1016/j.nima.2018.03.003>.
- 1006 [9] Nolan Espplen. “Physics and biology of ultrahigh dose-rate (FLASH) radiotherapy: a topical
1007 review”. In: (2020). DOI: <https://doi.org/10.1088/1361-6560/abaa28>.
- 1008 [10] M. Dyndal et al. “Mini-MALTA: Radiation hard pixel designs for small-electrode monolithic
1009 CMOS sensors for the High Luminosity LHC”. In: (2019). DOI: <https://doi.org/10.1088/1748-0221/15/02/p02005>.
- 1011 [11] M. Barbero. “Radiation hard DMAPS pixel sensors in 150 nm CMOS technology for opera-
1012 tion at LHC”. In: (2020). DOI: <https://doi.org/10.1088/1748-0221/15/05/p05013>.
- 1013 [12] K. Moustakas et al. “CMOS Monolithic Pixel Sensors based on the Column-Drain Architec-
1014 ture for the HL-LHC Upgrade”. In: (2018). DOI: <https://doi.org/10.1016/j.nima.2018.09.100>.
- 1016 [13] I. Caicedo et al. “The Monopix chips: depleted monolithic active pixel sensors with a column-
1017 drain read-out architecture for the ATLAS Inner Tracker upgrade”. In: (2019). DOI: <https://doi.org/10.1088/1748-0221/14/06/C06006>.
- 1019 [14] D. Kim et al. “Front end optimization for the monolithic active pixel sensor of the ALICE
1020 Inner Tracking System upgrade”. In: *JINST* (2016). DOI: [doi:10.1088/1748-0221/11/02/C02042](https://doi.org/10.1088/1748-0221/11/02/C02042).
- 1022 [15] L. Pancheri et al. “A 110 nm CMOS process for fully-depleted pixel sensors”. In: (2019). DOI:
1023 <https://doi.org/10.1088/1748-0221/14/06/c06016>.
- 1024 [16] L. Pancheri et al. “Fully Depleted MAPS in 110-nm CMOS Process With 100–300-um Active
1025 Substrate”. In: (2020). DOI: [10.1109/TED.2020.2985639](https://doi.org/10.1109/TED.2020.2985639).